N-HEPTANE AUTOIGNITION AND SPECIATION IN A NOVEL RAPID

COMPRESSION EXPANSION MACHINE

A Thesis

Presented in Partial Fulfillment of the Requirements for the

Degree of Master of Science

with a

Major in Mechanical Engineering

in the

College of Graduate Studies

University of Idaho

by

Samuel W. Van Horn

Major Professor: Kamal Kumar, Ph.D.

Committee Members: Dan Cordon, Ph.D.; Steven Beyerlein, Ph.D.

Department Administrator: Gabriel Potirniche, Ph.D.

May 2021

Authorization to Submit Thesis

This thesis of Samuel W. Van Horn, submitted for the degree of Master of Science with a Major in Mechanical Engineering and titled "*n*-Heptane Autoignition and Speciation in a Novel Rapid Compression Expansion Machine," has been reviewed in final form. Permission, as indicated by the signatures and dates below, is now granted to submit final copies to the College of Graduate Studies for approval.

Major Professor: _____ Date: _____

                Kamal Kumar, Ph.D.

Committee Members: _____ Date: _____

                Dan Cordon, Ph.D.

                _____ Date: _____

                Steven Beyerlein, Ph.D.

Department
Administrator: _____ Date: _____

                Gabriel Potirniche, Ph.D.

Abstract

This work examines the autoignition chemistry of fuel-lean *n*-heptane oxidizer mixtures. A Rapid Compression Expansion Machine (RCEM) was used to obtain both ignition delay times and study the stable intermediate species time evolution during the induction period. Ignition delay times for premixed fuel-oxidizer mixtures were obtained for compressed pressures between 3.0–5.5 bar and equivalence ratios (ϕ) between 0.20 and 0.50. The compressed temperatures were in the range of 592–763 K and included the onset of the negative temperature coefficient behavior for *n*-heptane under these test conditions. Trends for both the first-stage and overall ignition delay times as a function of temperature were obtained.

Additionally, the identification and quantitation of pre-ignition stable intermediaries were conducted. This was accomplished by rapid quenching of the reactions after the first-stage ignition phase in controlled time increments. A gas chromatograph-mass spectrometer system was used for the identification and quantification of stable intermediates. This work provides fundamental insights into the low-to-intermediate temperature oxidation kinetics of *n*-heptane using a new generation of electrically actuated and computer programmable RCEM.

Acknowledgments

Dedication

I want to dedicate this thesis to my family for their support and love during my graduate

studies. I would also like to dedicate this thesis to my wife. Her support, love, and patience

provided the means for me to pursue higher education.

Table of Contents

List of Tables

List of Figures

1 Introduction

1.1 Structure of the Thesis

Chapter 1 of this thesis provides a brief overview of the various experimental apparatuses used in combustion research to gather kinetic data from low to high-temperature conditions.

Chapter 2 discusses the unique design and key features of the new RCEM at the University of Idaho. This chapter will also cover experimental procedures, performance characteristics, and how data is collected from the RCEM.

Chapter 3 presents experimental results on the ignition delay of n-heptane under fuel-lean conditions. The variation of ignition delay times with compressed temperature, pressure, and equivalence ratio is examined. Reproducibility and range of physical combustion conditions attainable with the RCEM are presented. The numerical modeling approach for RCEM experiments is also presented. Comparison between the experimental measurements and model predictions for ignition delay times using detailed chemistry are shown.

Chapter 4 studies the oxidation of n-heptane by speciation data. The ability to rapidly expand (quench) the reactor core provides the ability to perform qualitative and quantitative analysis. Differences between measured concentrations and model predictions offer potential areas for model improvement at low-to-intermediate oxidation temperatures.

Chapter 5 concludes this study for the fuel n-heptane and provides recommendations for further studies using the new RCEM.

The work contained in this thesis has resulted in one paper presented at a regional conference of the western state's section of the combustion institute.

Chapter 3: S. Van Horn and K. Kumar "*n*-Heptane Autoignition and Speciation in a Rapid Compression Expansion Machine," Paper 911-0029, Fall Technical Meeting of the Western States Section of the Combustion Institute, Albuquerque, New Mexico, October 14 – 15, 2019.

1.2   Combustion Kinetics

Increasing energy demand, scarcity of fossil fuels, and stringent emission standards motivate researchers worldwide to study alternative fuels and advanced energy conversion concepts. A part of this research is striving to understand the chemical reactions involved in the oxidation of fuels. Studies investigating reaction rates and mechanisms have been the focus of combustion research to address practical problems. Such problems include the pollutants emitted from current combustion engines and improved engine performance. Combustion modeling has significantly advanced due to the establishment of combustion chemistry aided by kinetic data availability.

Accurately modeling combustion systems requires a detailed kinetic mechanism. A detailed kinetic mechanism for large carbon number hydrocarbon fuel incorporates thousands of chemical reactions and several hundred intermediate species. Kinetic mechanisms have been tested against experimental data from a variety of different experimental apparatuses and combustion conditions. This allows for models to predict the performance of new combustion systems. Advanced combustion systems continually strive to improve performance by drawing insights from advances in modeling. Well-designed laboratory experiments help validate the combustion chemistry in the mechanism. Experimental observations that fall outside of a proposed model's prediction capability inspire further refinement and additional constraints.

Experimental data obtained at engine-relevant combustion conditions are particularly important to assess the detailed chemical mechanism's effectiveness. It is desirable to get useful experimental data from multiple devices that can closely duplicate these conditions. The difficulty arises in interpreting the data from such apparatuses due to the effects of fluid motion on combustion chemistry. Researchers have designed several types of laboratory devices that

minimize the effects of fluid motion on chemistry and facilitate the study of combustion kinetics. Such devices include plug flow reactors, jet-stirred reactors, shock tubes, and rapid compression machines (RCM's). These tools can retrieve data across a wide range of combustion conditions, depending on the device being used.

A discussion of each apparatus mentioned previously will provide a context on each machine's merits and capabilities. Then a brief history of the development of the RCM will be presented.

1.3   Homogeneous Combustion Apparatuses

1.3.1   Plug Flow Reactors

A plug-flow reactor represents a channel-type reactor with no radial variation in temperature or species concentration [1]. The assumption is that the axial directional mixing of the fuel does not occur, given that molecular or turbulent mass diffusion is negligible in the flow direction. For a given inlet condition, fuel and oxidizer are perfectly mixed, and the mixture reacts as it travels down the tube. The variables describing this reacting system are, therefore, only a function of the axial coordinate. Pressure and velocity are related by Euler's equation by assuming that the surfaces inside the tube are frictionless [2]. Species and temperature data can be retrieved at various axial stations to examine the progress of reactions.

1.3.2   Jet-Stirred Reactor

The Jet-Stirred Reactor (JSR) is a widely used tool in combustion kinetic research [3]. The apparatus is typically a spherical-shaped reactor with several jet injection nozzles installed inside. Fuel is diluted with inert gas and then introduced into the reactor. The fast mixing of the reactants allows for the assumption of a homogeneous mixture inside the vessel. The reactor volume is also adiabatic and can tolerate temperatures up to 1900 K [4]. The system is operated at constant pressure, steady-state, and can provide varying residence times. Due to the assumption of working at steady-state, mathematical models used to simulate the JSR are non-time dependent and primarily consist of coupled nonlinear algebraic equations [5].

1.3.3   Shock Tubes

The shock tube is a research apparatus used to study autoignition characteristics at relatively higher pressures and temperatures for reactive fuel mixtures. It consists of a tube divided into two sections, a driver and a driven section. The driver section contains an inert gas at high

pressure, whereas the driven section contains the reactants at low pressure. A thin diaphragm separates the two areas. A sharp needle-like object typically ruptures the diaphragm. The sudden rupture creates a moving normal shock wave that propagates into the driven section. This moving normal shock wave heats and pressurizes the reactants as it passes through. The ignition delay time is measured after the passage of the reflected shock through the reactant gases. Shock tubes have achieved temperatures of up to 1300 K and 80 bar [6]. Other studies have shown that shock tubes can reach temperatures as high as 5000 K [7]. Measurable chemical conversion and ignition delay times are limited to short intervals due to boundary layer effects [8]. Therefore, shock tubes are limited in operating range to short induction periods.

1.3.4   Rapid Compression Machines

An experimental apparatus called a rapid compression machine (RCM) simulates a combustion engine's single compression stroke. A typical RCM consists of a piston that is attached to a rod. A pneumatic system typically drives the piston rod. A fuel-air mixture is deposited into the cylinder, where the piston will rapidly compress the mixture. The typical time to compress the premixed fuel-air mixture is between 40-100 milliseconds. Post compression, the piston is held fixed at the top dead center (TDC) by a pneumatic system. At the end of compression (EOC), elevated temperature and pressure in the range of 500–1200 K and 7–60 bar, respectively, are obtainable [9, 10]. An isentropically compressed adiabatic core is assumed post-compression in the reactor core [11]. Changing the EOC conditions can be achieved by varying the compression ratio, initial pressure, temperature, and fuel mixture composition. Experimental data obtained from an RCM primarily consists of pressure traces as a function of time. RCM's have also been used to investigate the low-temperature combustion (LTC) and autoignition

chemistry for alkanes [12], alcohols [6], and even jet fuels [13]. An RCM gives direct measurements of pressure histories as a function of time.

1.3.4.1 History of Rapid Compression Machines

K.G. Falk developed the first RCM in 1906 to determine the ignition temperature of hydrogen-oxygen mixtures [14]. His unique design consisted of a vertical piston and rod made of one piece driven by a falling weight. The falling weight would impact the piston rod and propel the piston into the reactive cylinder and compress the reactive fuel mixture. The apparatus was capable of different compression ratios by merely changing the mass or height. The final height of the piston was recorded and used to calculate the ignition temperature. RCM's have improved in experimental capability and complexity since Falk's first experimental apparatus. Still, the overall operation is the same by using an external force to drive a piston, followed by an immediate arrest of piston motion.

Over the next 60 years, RCM's abilities to retrieve combustion data grew to include optical diagnostics to explain flame propagation, ignition delay time, pressure histories, two-stage ignition, and the presence of a negative temperature coefficient region. In 1960, L.H.S Roblee, Jr. conducted experiments with an RCM investigating the chemical histories of the high pressure and temperature reactions using a quenching chamber attached to the RCM [15]. This quenching chamber provided a means to rapidly expand the control volume at EOC and cease fuel oxidation. Capturing the reactants was accomplished by a diaphragm's rupture through pressure buildup or by a mechanical probe. By rapidly expanding the volume after EOC (during the ignition delay period), the reactant's chemical progression froze (due to shock cooling), allowing for a qualitative analysis of the partially oxidized reactive fuel mixture. This capability to retrieve such chemical data opened the ability to investigate the progress of reactions.

Depending on the apparatus's design, they could recover other ignition data but with added design complexity. The current generation of RCM's typically employs a pneumatic driving force to initiate and sustain piston motion and a hydraulic dampening mechanism to rapidly decelerate and stop the piston at the end of compression. These new RCM's provide higher compression ratios and faster compression times than the older generation of RCM's [9].

1.3.4.2 Currently used RCM's

Current RCM's used for combustion research will be discussed to make apparent the unique design features of the novel RCEM used in this study. Critical components for each RCM will be discussed and analyzed.

The RCM at Karlsruhe Institute of Technology, Institute of Technical Thermodynamics, Karlsruhe, Germany, uses a pneumatic actuator connected to a knee-lever through a rod. Another rod connects the piston to the knee lever, and as the pneumatic actuator extends, the knee lever pushes the piston into the cylinder. This RCM has operated with a compression ratio (CR) of 7.2 – 12.1 and has achieved a compressed pressure and temperature of 10.4 bar and 839 K using a nitrogen/oxygen mixture. The RCM at Karlsruhe Institute of Technology was used to study polyoxymethylene dimethyl ether fuels and their possibility of being used as either blends or a complete substitute for diesel fuel [16]. This machine has been able to obtain ignition delay times up to 35 ms.

The rapid compression machine at the Université des Sciences et Technologies de Lille, France, has an overall compression ratio of 9.28 and has conducted studies requiring compression times between 20–60 ms [17]. The driving mechanism employs a right-angle design to which a mechanical device actuates the piston. Another piston then actuates the mechanical device. The RCM is configured to record pressure histories and has optical accessibility into the reactor core

chamber. It is equipped with pressure transducers and light emission recording cameras. The machine is also capable of rapid sampling for the analysis of stable intermediate species. It has been used for extensive studies of alkanes, alkenes, aromatics, methyl esters, and other combustion research fuels. The RCM cylinder wall is capable of heating to allow for elevated initial temperatures.

State Key Laboratory of Engines (SKLE), Tianjin, China, has developed an RCM to study the phenomenon of knock-in combustion engines. The RCM employs pneumatically driven and hydraulically stopped mechanisms. The RCM has an adjustable compression ratio between 10 and 21 and has achieved a compressed pressure of 60 bar. Adjustment of the stroke and clearance volume allows for the change in the compression ratio. The RCM can monitor the piston movement using a motion pickup transducer and uses a flat piston design to simulate more closely actual engine conditions. The RCM is also capable of flame propagation studies by using a quartz window attached at the end of the reactor cylinder in addition to pressure history studies [18].

Pneumatic and hydraulic systems accelerate and decelerate the piston motion for the RCM's at the University of Connecticut, Storrs, CT, USA. The device can have a compression time of 30 ms and a compression ratio between 7–17. Stroke travel and top dead center (TDC) clearance are adjusted to change the compression ratio (CR). The bulk of the compression occurs between 25–35 ms. Compressed pressures and temperatures were measured to be as high as 40 bar and 900 K. Using this RCM, surrogate fuel autoignition has been investigated [19, 20].

The rapid compression machine at Yonsei University, Seoul, South Korea, uses pneumatic power to move the piston from the start of compression (SOC) and hydraulic power to stop the piston at the top dead center (TDC). Transparent windows allow for optical analysis of the

reactor. The machine can have a max compressed pressure and temperature of 50 bar, and 1100 K. Compression ratios are between 13–21. The compression time ranges from 15–40 ms. The piston incorporated a creviced piston design to limit the effects of fluid motion. This machine investigated the two-stage ignition of hydrocarbon autoignition and new gasoline surrogates [21].

These RCMs incorporate different features and abilities that took years to develop. Many of the RCMs can adjust compression stroke, and many have used the creviced piston design to limit the effects of the roll-up vortex through fluid motion. These RCMs can define the core region and rapidly compress the fuel mixture. A few RCMs are also capable of additional studies that include flame propagation (through quartz windows) and speciation (quenching the reactor core with a fast sampling apparatus).

This brief survey of existing rapid compression machines includes only a few machines and is by no means an exhaustive summary. An excellent review on design features, advancements, capabilities, and utilization of RCM's can be found in the work of   Sung and Curran [9].

1.4   Advantages and Challenges with Rapid Compression Machines

Due to the interaction between fluid motion and combustion reactions, experimental apparatuses that generate homogeneous conditions allow a more straightforward interpretation of kinetic data. On the other hand, a device that can simulate real-world combustion conditions and engine dynamics can provide more application-relevant ignition data. An RCM is an experimental apparatus designed to simulate a single compression stroke of an internal combustion engine. Reaction chamber pressure data is measured directly using a dynamic pressure sensor and used to determine ignition delay time. RCM's are preferable for experiments in the millisecond time scale and provide insight into the autoignition phenomenon between 600–1100 K. The RCM can be used to study two-stage ignition, negative temperature coefficient region (NTC) of the reaction rate, and other fuel-specific ignition properties.

RCM apparatuses have their unique challenges. The design and build of various RCM's can have notable differences that have a significant impact on the machine's performance. Current research efforts have not established a standard for the RCM combustion research apparatus design, which has resulted in many RCM's performing similar combustion experiments that provide different results. Differences between the piston head's design and the reactor cylinder's surface-to-volume ratio are the main contributors to differences in fluid motion and heat loss effects in various RCM's. Currently used RCM's also lack specific controls that hinder the quality of chemical kinetic data. Most RCM's today are mechanically operated and use mechanical impact mechanisms to stop the piston's motion.

Such devices significantly add to the background noise due to the apparatus vibrations and create a more significant challenge in interpreting experimental data. Also, the mechanical design of most RCM's used today cannot directly measure the piston's position from the start

to the end of compression. The percent of pressure rise over initial pressure defines the position of the piston for RCM's. Visual observations based on pressure traces are the primary methods for determining the end of compression (EOC). This approach complicates numerical models that require volume profiles from the experiment and significantly affect the results' reproducibility.

The brief review of existing RCM's demonstrates the utility of these devices for low-to-intermediate temperature autoignition studies. However, the current generation of RCM's share some common features which require attention to enable accurate kinetic studies. Among the critical concerns with the existing designs are:

1. The current generation RCM's are all mechanically operated devices and use mechanical impact to arrest piston motion. This leads to significant noise in the experimental data on account of machine vibration, making *data interpretation and diagnostics a challenge* [9].

2. The mechanical nature of these machines makes it *impossible to identify both the start and the end of compression unambiguously*. The problem of determining the onset of compression is circumvented by adopting arbitrary references such as a given percent pressure rise over initial conditions and assigning $t = 0$ at the end of compression. The identification of the end of compression is very much dependent on visual observations or the determination of inflection points in the pressure trace.

3. The current generation of RCM's have uncontrolled motion and are *unable to provide any direct measure of piston velocity and position*. The reactor volume profiles are indirectly inferred from the pressure traces by empirical fits assuming an acceleration and deceleration time [22, 23]. This issue becomes important when carrying out computer modeling with

detailed chemistry where exact volume-time history must be specified. *The lack of motion control significantly affects the reproducibility of results.*

The current RCEM alleviates much of the aforementioned operational issues associated with the previous generation of rapid compression machines. Modern developments in electrical drive technology and electronic control systems have been used to eliminate hydraulic and pneumatic systems. This extends the operational envelope for the current device by allowing a *programmed compression as well as expansion,* which is not possible with most existing machines. The design goal of the RCEM is to enable detailed species diagnostics in addition to global measurements of ignition delay.

While some parameters can be measured directly from the RCM during the experiment, direct measurement of the compressed temperature (T_c) at the end of compression (EOC) is not possible. The T_c , to a first approximation, is computationally determined using the adiabatic compression relation. The compressed temperature can then be calculated at the top dead center (TDC) by the following relation.

$$\int_{T_o}^{T_c} \frac{\gamma}{\gamma - 1}\frac{dT}{T} = \ln\left(\frac{P_c}{P_o}\right) \tag{1.1}$$

In the equation above, P_c is the compressed pressure, P_o is the initial pressure, T_o is the initial temperature and γ is the ratio of specific heat at constant pressure to specific heat at constant volume. The mixture specific heat in equation 1.1 is a function of temperature, and this variation needs to be accounted for as the system compressed temperature changes during compression. The system is not genuinely adiabatic due to heat loss to the surrounding inner reactor cylinder, piston head, and front flange surfaces. The measured pressure at EOC (P_c) is lower than the corresponding adiabatic value for a given compression ratio. An empirical adjustment

(increase) in the reactor volume is used to match the experimental pressure value for modeling purposes. The post-compression pressure drop is also empirically modeled by assuming a time-varying slow expansion of the adiabatic core. A detailed description of this approach is provided in the section on numerical modeling in chapter 3. An essential factor in obtaining meaningful data from an RCM is the ability to establish a thermodynamically well-defined homogeneous reactant mixture at and after the end of compression.

1.5   Research Objectives

Given the challenges associated with the current generation of rapid compression machines, a new RCEM was designed and fabricated at the University of Idaho to study autoignition kinetics. The novel RCEM employs a new programmable driving mechanism that allows ease of use and variable compression ratios without mechanical manipulation of the apparatus itself. The driving mechanism allows for two different operating modes to obtain either ignition delay data through rapid compression (RCM) or speciation samples through rapid compression and rapid expansion (RCEM). This machine enables greater flexibility and precise control over operating conditions and incorporates features that provide the opportunity to obtain long ignition delay times at low-to-intermediate temperatures.

This study uses an RCEM to understand the oxidation of a gasoline primary reference fuel (PRF) component n-heptane (n-C$_7$H$_{16}$). Ignition delay is affected by varying compressed pressures, temperatures, and equivalence ratios. Repeatability of ignition delay data is essential for good qualitative and quantitative analysis. A speciation study using a gas chromatograph-mass spectrometer (GC-MS) aided by quantitative calibration curves is used to measure the concentration of the various stable intermediate species identified from the experiments and provide a detailed understanding of oxidation kinetics. There is a lack of data looking into the primary reference fuel (PRF) oxidation pathways at low temperatures utilizing speciation measurements. Such data at low combustion temperatures can aid further development of LTC systems.

Numerical models simulate the performance of the RCEM for ignition delay data and also validate the machine's ability to quench the reactions during the induction period. Experimental results were compared against model predictions using the detailed n-heptane mechanism

(Version 3.1) from Lawrence Livermore National Laboratory [24-26]. Comparing the experimental data against the modeling calculations can help determine the necessary refinements and changes needed to improve the chemical kinetic mechanism for n-heptane.

2 Experimental Facility

2.1 Introduction

An RCM is a laboratory tool used to simulate a single compression stroke of an internal combustion engine. The rapid compression of reactants results in elevated pressure and temperature after the end of the stroke. Once the piston reaches TDC, the piston is either locked into place or rapidly retracts at a designated time during the ignition delay period. Acceleration and deceleration of the moving masses can generate large inertia forces, resulting in induced vibrations and background noise [9]. The effects of vibrations on RCM's can impact the ability to maintain a constant volume at TDC.

Furthermore, vibration and background noise can lower the experimental data quality and lead to mechanical damage to the RCM apparatus. Various controls allow the machine to avoid overshoot, rebound at the TDC position, and maintain a constant volume chamber [9]. Over the years, new RCM designs have improved and increased operating capability and durability. Significant improvements to the driving mechanism and controls minimize the piston's rebound at TDC and vibrations. Early RCM's primarily used kinetic energy in the form of a falling weight [14] to move the piston. Currently used RCM's use a pneumatic system to move the piston. The pneumatic driving system has achieved fast compression times and high compression ratios [9]. Further details on the advances in RCM technology and its use for chemical kinetic research can be found in the work of Goldsborough et al. [27] and Sung and Curran [9]. Any new machine must rapidly compress the fuel mixture quickly and provide reasonably large test times. Additional useful features could include varying compression stroke, extraction of reacting mixtures for specie analysis, and optical accessibility.

2.2   Current Rapid Compression Expansion Machine Configuration

The novel RCEM design used in this work encompasses a radical change from the established

mechanisms used to drive and arrest the piston from start to end of compression. The driving

mechanism consists of a stainless-steel thrust rod with enclosed rare earth magnets and is

started, moved, and stopped electrically. The piston is made of aluminum and encompasses a

creviced design similar to previous RCM configurations [23, 28]. The maximum stroke is 12.5

inches. The reactor cylinder is made of aluminum and is attached to the motor using steel

mounts. Between the reactor cylinder and the motor are the bearings, which allow the piston to

move. The thrust rod is driven by a forcer that encloses a motor coil and integral position

sensing electronics. The motor delivers a continuous driving force of 1000 N with peak

accelerations of over 150 m/s^2. The CANopen communication system works in conjunction

with the forcer [29]. This communication system is a standardized embedded network with

flexible configuration capabilities.
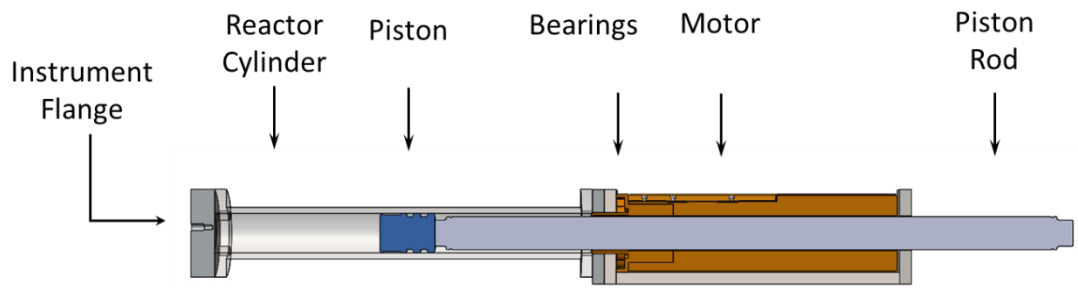
Figure 2.1: Schematic of the rapid compression expansion machine (RCEM)

The reactor head is equipped with a pressure sensing and charge feed port. A piezoelectric

pressure transducer (Kistler 6052 C) coupled to a charge amplifier (Kistler 5011B) measures

the reactor dynamic pressure. The initial feed pressure (P_0) is determined utilizing a separate

absolute pressure sensor. A schematic of the RCEM apparatus discussed above is shown in

Figure 2.1. The current apparatus is configurable as a fully controllable, high-speed, variable volume piston reactor capable of time-resolved speciation diagnostics. It is capable of a rapid compression stroke and an equally fast piston retraction. The operations to rapidly compress and expand are computer-controlled. An infinitely variable compression ratio of up to 20 can be achieved with a positioning accuracy of 69.53 microns (one encoder pulse). Fully programmable piston velocities in excess of 5 m/s have been achieved in the current work. The motion control system allows for precise positioning of the piston aided by encoder feedback.
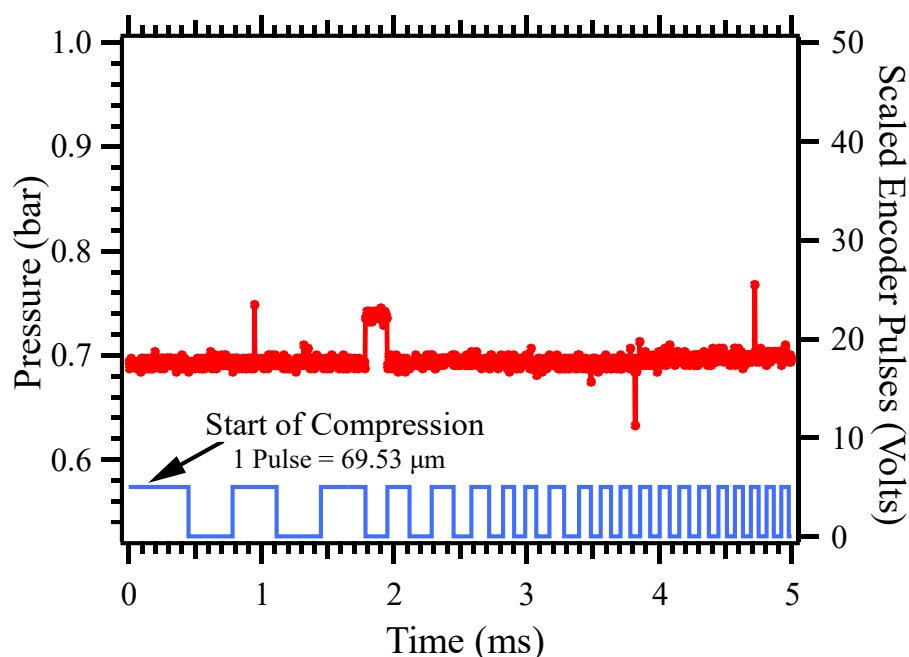
Figure 2.2: Initiation of piston motion (SOC) with clear identification of start time (t=0).

Clear identification of the start of compression and the ability to track motion progression is shown in Figure 2.2. The figure shows two different vertical axes. The left axis represents the pressure (red line) inside the reactor cylinder close to the start of the piston motion. The right axis represents the scaled encoder pulses (blue rectangular waves) that indicate the piston's movement. The horizontal axis indicates the time of the system. Widely spaced pulses indicate a little or no motion, whereas acceleration or deceleration of the piston is manifested as

increasing or decreasing pulse width, respectively. Figure 2.2 also shows the first encoder tick at the piston's starting position before rapid compression. As the width of the pulses decreases, the pressure of the system begins to increase. Eventually, the piston accelerates, and spacing between encoder pulses becomes extremely small.

We have conducted experiments using our RCEM apparatus to illustrate some of its key distinguishing features in the normal RCM mode (without quick expansion). The results from a reactive run for an *n*-heptane oxidizer mixture are shown in Figure 2.3 for a compressed pressure of 6 bar. The definitions of the first (τ_1) and second-stage delay (τ_2) based on the maximum rate of pressure rise are also shown in the plot. Note that position feedback in the form of encoder pulses is available throughout the experiment. This provides us with an unambiguous reference for the start of motion and the end of compression (EOC). The start of compression (SOC) is easily identified and is shown in an expanded view in Figure 2.2 above. The end of compression can also be easily identified in the pulse train in Figure 2.3. It can also be seen that the control system does an excellent job of maintaining constant volume conditions after the end of compression. In the case of pneumatically driven machines, these two reference times are rather arbitrarily defined due to a lack of position feedback.

The encoder pulses appear as a solid blue bar on the horizontal axis until the piston reaches EOC (88.365 ms). A constant volume reactor chamber condition after EOC is established, as shown by the very few encoder ticks (~15 pulses) between 88.365–127.326 ms. The reactive fuel mixtures autoignites at 127.85 ms, as seen by the rapid rise in pressure.
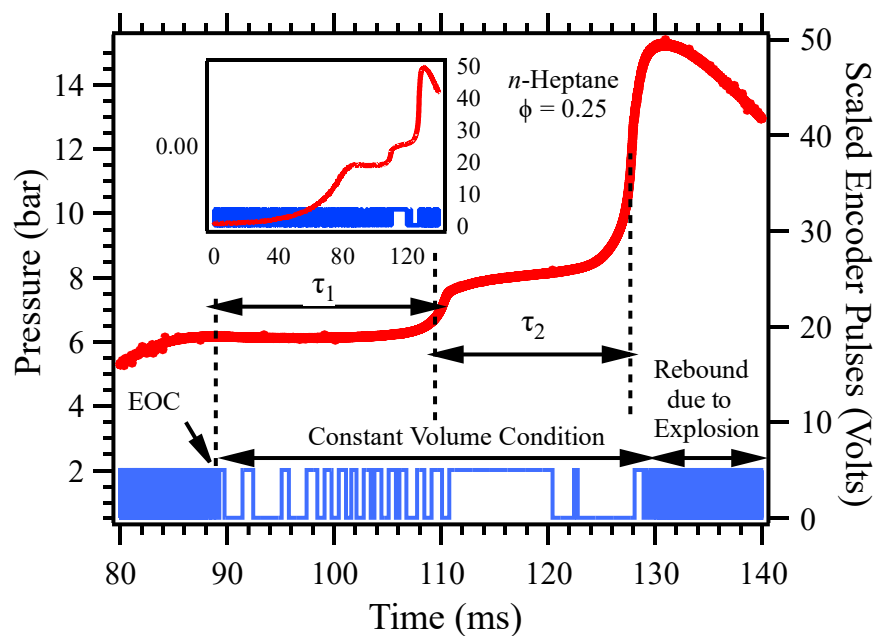
Figure 2.3: A reactive run with position feedback

The position feedback enables the reconstruction of the piston's trajectory as a function of time. The feedback is useful in simulating the system using detailed chemistry where the volume as a function of time is an input parameter.

Figure 2.4 demonstrates the reconstruction of the reactor volume from the piston displacement (encoder pulses). The corresponding reactive pressure trace is on the right axis for the figure. This direct measurement of the change in volume over time leads to more accurate numerical modeling of experimental reactive runs.
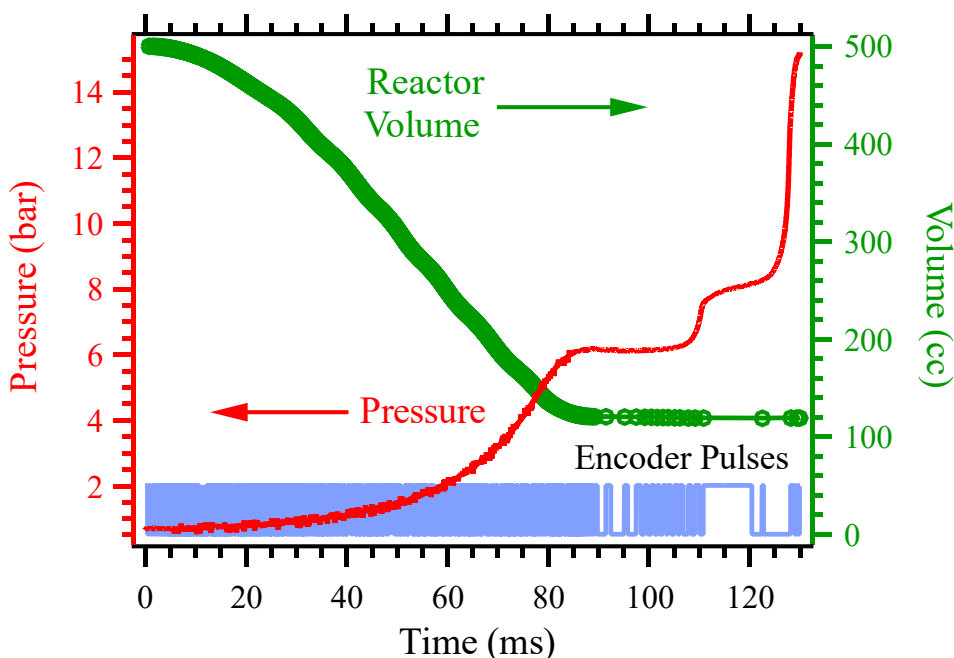
Figure 2.4: Reactor pressure and volume variation with time.

This machine can operate in two modes. The first mode is similar to a traditional RCM with pure compression. The second is with both rapid compression and a programmable expansion. The expansion time can be varied after EOC, allowing multiple partially reacted gaseous samples to be collected. This feature avoids reflected shocks during the bursting of diaphragms in conventional sampling apparatuses, which can re-initiate reactions in the quenched gas [15]. This ability to expand the reactor core utilizing rapid expansion (quench) enabled experimental runs to be highly reproducible and eliminated disassembly, installation, and re-assembly after each run which must be done for conventional sampling apparatuses. As a result of limited mechanical adjustments after each experimental run, the operational speed and efficiency are

significantly enhanced. After quenching the reactor contents, the products are extracted by opening the instrument flange valve, pushing forward the reactor cylinder very slowly, and collecting the gaseous sample in a syringe.

During regular RCEM operation, the piston's rapid compression motion leads to velocity gradients in the fluid at EOC. This leads to the development of flow structures that take the shape of a roll-up vortex. The roll-up vortex leads to mixing cold gases along the inner reactor cylinder wall with hot gases in the reactor core region. This mixing creates a non-uniform temperature field. The assumption of a homogeneous reactor temperature field may, therefore, not be satisfied at the EOC. Minimizing the roll-up vortex can be accomplished by implementing a crevice machined into the piston sidewall. This design allows cold gases to flow into the creviced volume and helps suppress the roll-up vortex. A non-homogeneous temperature field would introduce discrepancies in the measured data.

The piston crevice in the current RCEM has been designed to minimize the roll-up vortex and enable long test times of more than 100 milliseconds. Results from a preliminary laminar, axisymmetric, non-reactive simulation at the end of compression are shown in Figure 2.5. The simulations were done using Ansys Fluent [30], and the encoder position output from the current RCEM was used to specify the piston motion profile. Figure 2.5 shows that the temperature field is nearly homogeneous within the reactor core, with the roll-up vortex confined to a narrow region close to the piston face. A constant temperature wall boundary condition was used for the simulations. Additional refinements will be done by solving the conjugate gas-solid heat transfer CFD problem in future research.

The improvements in position control, velocity specification, and heat loss modeling are expected to reduce the facility-dependent effects. Such machine-specific peculiarities make it challenging to compare data across machines operated by different research laboratories.
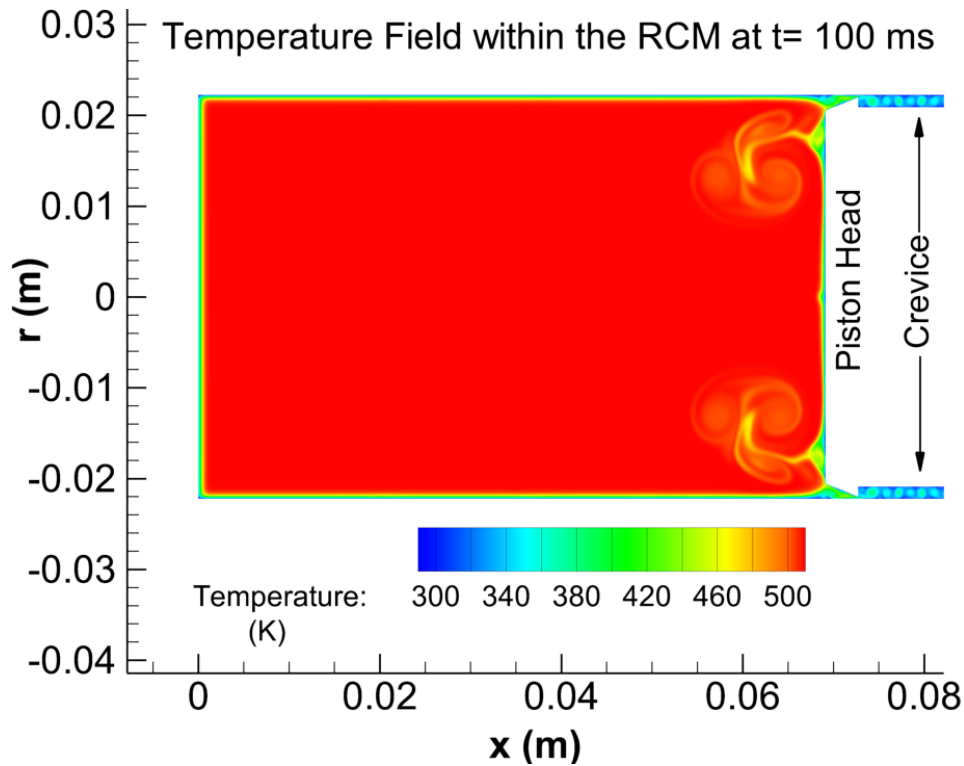
Figure 2.5: CFD results for the non-reactive temperature field in the current RCEM.

The development of this experimental tool is a step in advancing the RCEM technology toward a higher diagnostic capability level.

To summarize, the key benefits from the current RCEM development efforts are:

1. A clearly defined start and end of compression with position feedback

2. Ability to program a piston velocity profile with known acceleration and deceleration

3. An infinitely variable compression ratio for access to thermodynamic states not previously possible.

4. Automation of rapid species sampling at pre-selected times and for controlled durations

5. Precise synchronization to external events (laser/camera triggering) through available digital I/O.

2.3   Experimental Methods

The RCEM experiments in this work were used to obtain ignition delay and time-resolved speciation data. A 12.41-liter stainless steel vessel equipped with vaned magnetic stirrers was used to mix the fuel and oxidizer thoroughly. The oxidizer composition is determined based on the manometric readings for the fill pressure for each component. The oxidizer used for this experiment comprised ultra-high purity argon and oxygen in the molar ratio of 1:3.76. The use of argon as an inert enabled higher compressed temperatures than would have been possible with nitrogen under similar compression ratio conditions.

The desired amount of liquid fuel (*n*-Heptane ≥ 99% purity) was weighed and injected into the mixing tank. A manometer measured partial pressures in the stainless-steel vessel. A manually operated valving system connected this stainless-steel vessel to the RCEM reaction chamber. Additional valving system on the RCEM front flange enabled the extraction of quenched products from the reactor.

The operating procedure consists of first preparing the premixed charge in a stainless steel vessel. This is followed by allowing the RCEM and the charge to stabilize to the desired temperature set-point (T_0) for approximately 1 hour. The reactor chamber is then vacuumed out and retracted to the starting position. The piston is held in place by powerful magnets while the pump maintains a vacuum in the reactor cylinder. The reactor chamber is filled to the desired initial pressure (P_0) by connecting it to the mixture preparation vessel. The initial fill temperature, pressure, and mixture composition (γ) completely specify the reactants' initial state. The compressed final state at the EOC, assuming that no reaction occurs during compression, is a function of the compression ratio for a given mixture composition. The compression ratio is programmatically varied using a code developed as a part of this work

[31]. Another approach to changing the final state would be to alter the oxidizer mixture composition (γ) while maintaining a fixed compression ratio. Note that the temperature calculations in this work consider the temperature variation of the specific heat ratio (γ) with temperature.

2.4   Performance Characterization of the RCEM

The performance of this RCEM was tested for both the expansion and compression events. The machine functioned flawlessly and provided a controlled compression and expansion in the millisecond timescale. The experimental pressure traces for five different compression and expansion events are shown in Figure 2.6. The device was programmed to compress atmospheric air and quench/expand in increments of 50 ms. The geometric compression ratio was 4.44, which should result in a compressed pressure of ~8.07 bar. The reduced pressure is due to instrumentation port dead volumes and reactor head o-ring thickness.

Additionally, heat loss from the walls is the primary cause of non-adiabatic compression. This reactor used a custom sealing arrangement that permits a stable post-compression test duration of *at least* 200 ms, as seen in the figure. Currently available machines usually achieve half that test duration.
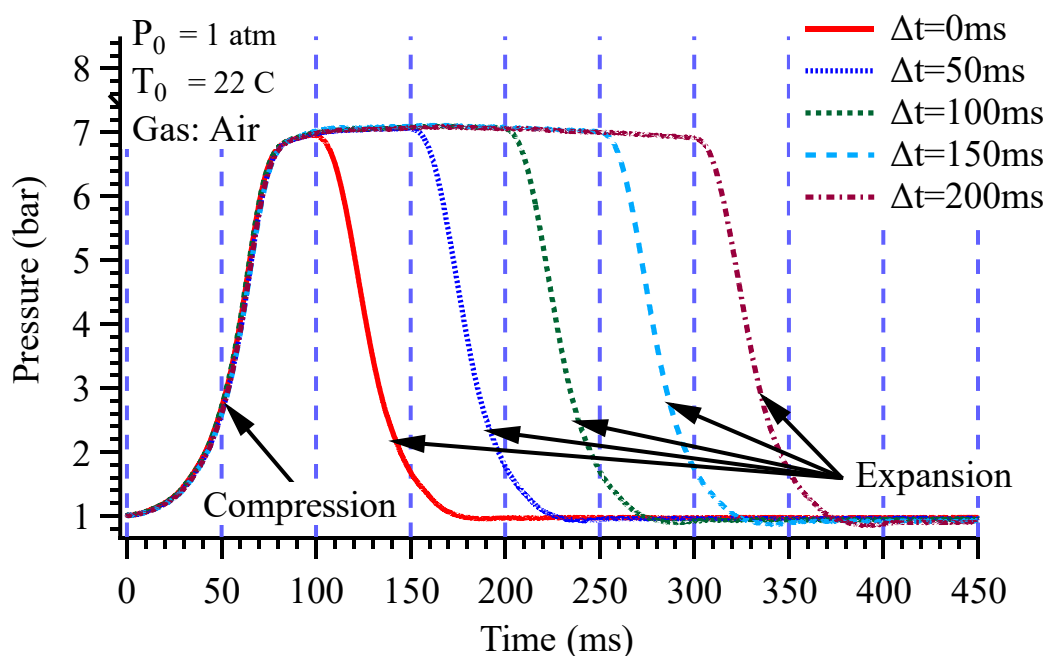
Figure 2.6: Pressure traces showing inert compression and expansion strokes.

If the end of compression (EOC) conditions are adequate to initiate ignition, then a time delay is manifested between the EOC and fuel mixture's autoignition, as shown in Figure 2.7. The definition of ignition delay is the time between EOC and the autoignition of the reactive fuel mixture. Ignition delay is one of the global measurements used to understand hydrocarbon fuel oxidation. A specific characteristic of *n*-heptane oxidation is the presence of two-stage ignition. Ignition delay will be one of the primary focuses of this study.
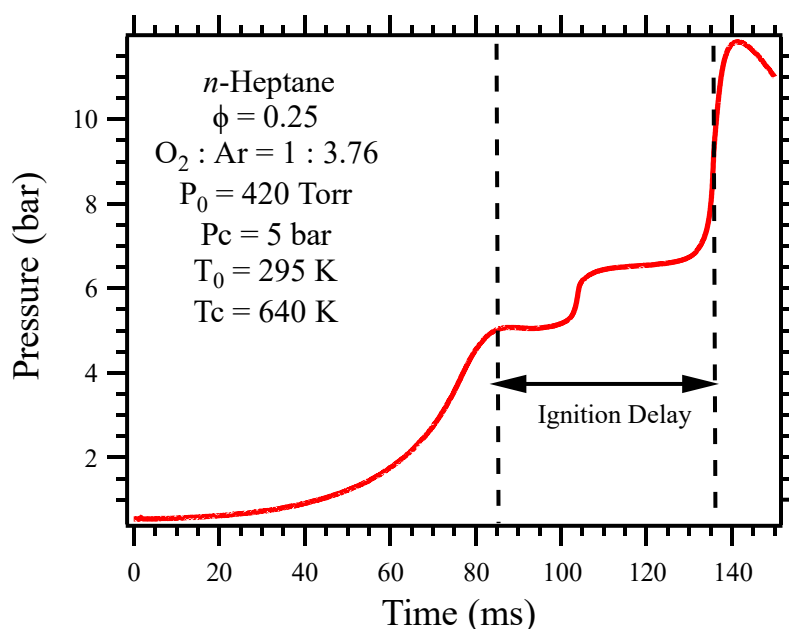
Figure 2.7: Typical pressure trace of the reactive fuel mixture.

An essential feature of any experimental device is its ability to generate reproducible data. Figure 2.8 show three experimental runs conducted under identical conditions for the time interval from the start to the end of compression. A complete set of experimental runs, including the autoignition event, is shown in Figure 2.9, which illustrates the essential characteristics of the RCEM performance. The pressure-time history profiles in Figure 2.8 and Figure 2.9 demonstrate a high level of repeatability between experimental runs, as seen from the overlapping pressure traces. This is evidence to support the assumption of repeatable

combustion conditions being attained for each experimental run. The pressure traces do not exhibit any vibrations at the end of compression.
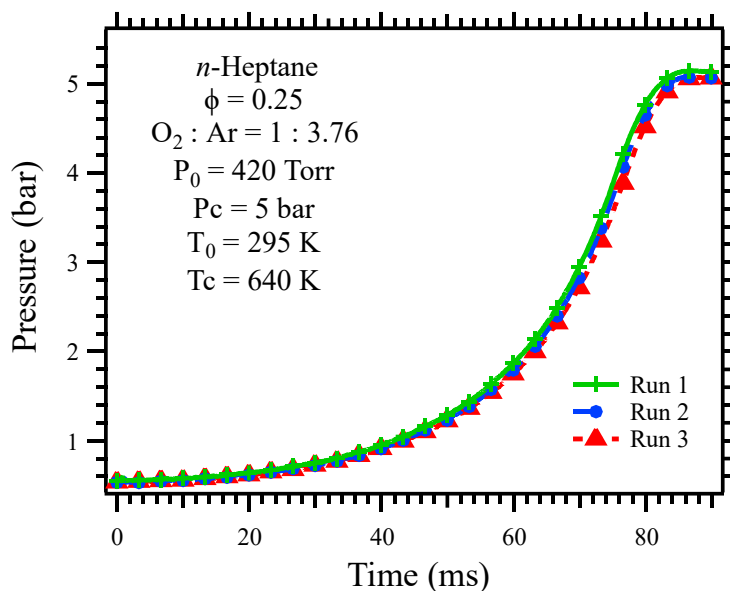
Figure 2.8: SOC to EOC repeatability.
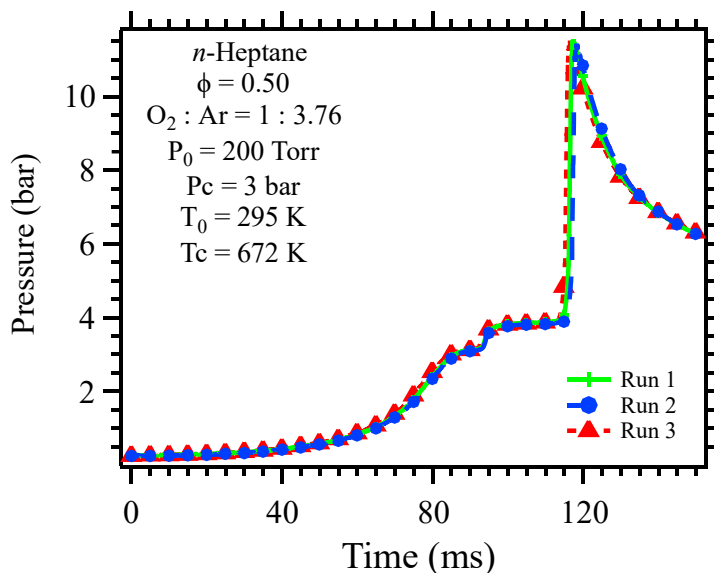
Figure 2.9: Repeatable pressure histories for reactive fuel mixture autoignition.

3   Autoignition Results for *n*-Heptane

3.1   Introduction

The combustion characteristics of *n*-heptane over a wide range of conditions have been examined in several prior studies. They include investigations on laminar flame speeds [32], flame structure [33], ignition delay times in shock tubes and rapid compression machines [34, 35], speciation histories from jet-stirred reactors [3], and combustion in research engines [36]. The rapid compression machine (RCM) has been a preferred laboratory tool for fundamental autoignition studies in the low-to-intermediate temperature range. Several previous studies have reported on the autoignition of *n*-heptane in RCM's [21, 37-43]. Its blends with other fuels have also been investigated [38, 44-47]. Ignition delay times obtained using an RCM are among the most widely studied global combustion response. The apparatuses' past design considerations limited their ability to retrieve more detailed combustion data. Its use in tracking species time histories has been relatively limited. Species time histories provide a higher level of rigor in the validation process for chemical kinetic mechanisms. The pre-ignition intermediaries formed during the induction period govern the autoignition process. Few studies have attempted to understand these intermediate species' time evolution before and during the autoignition event. Therefore, typical low-to-intermediate temperature validation targets for chemical kinetic models are mostly limited to autoignition delay times. The time evolution profile of intermediaries during the induction period is precious. It provides another target in addition to ignition delay times to improve and refine chemical kinetic mechanisms.

This work presents the autoignition of *n*-heptane and identifies and quantifies stable intermediaries during the induction period. It uses a new rapid compression expansion machine

(RCEM) and obtains ignition delay data over a wide range of compressed temperatures, pressures, and equivalence ratios.

Experimental values are compared to the results obtained from computer simulations using detailed chemistry. The *n*-heptane mechanism from Lawrence Livermore National Laboratory (LLNL Version 3.1) [24-26] is used for the chemistry set. The simulations compare the global ignition delay times as well as the evolution of the entire pressure-time histories, including the compression stroke. The simulated concentrations of intermediate species were also tracked during the induction period.

.

3.2 Numerical Model

3.2.1 Governing Equations

Numerical modeling of the RCEM was carried out using the Ansys Chemkin-Pro Package [48] and uses the zero-dimensional closed homogeneous batch reactor model with finite-rate chemistry. The governing equations for mass, species, and energy conservation implemented in the simulations follow those for an adiabatic system with a time-varying reactor volume described by Lutz, Kee, and Miller [49] and are stated in equations (3.1)-(3.3) below.

The condition for a closed system with a fixed mass can be written down as

$$m = \sum_{k=1}^{K} m_k = \text{constant} \text{ or } \frac{dm}{dt} = 0 \qquad (3.1)$$

Where m is the total mass obtained by summing over the total number of species (K) present in the system, with m_k representing the mass of the k_{th} specie. The individual species production or consumption ($\dot{m}_k$) involves its molar production rate ($\dot{\omega}_k$) by the elementary reactions and is expressed as:

$$\frac{dm_k}{dt} = V(t)\dot{\omega}_k W_k \qquad (3.2)$$

Here V is the system volume and W_k the molecular weight of the k_{th} specie. The energy equation for a closed system assuming a calorically perfect gas with a mean specific heat of c_v can be shown to be:

$$c_v \frac{dT}{dt} + p \frac{dv}{dt} + v \sum_{k=1}^{K} e_k \dot{\omega}_k W_k = 0 \qquad (3.3)$$

The quantity e_k represents the internal energy of the k_{th} specie and under the calorically perfect assumption we can state that $de_k = c_{v,k}dT$. The mean specific heat is evaluated as $c_v = \sum_{k=1}^{K} Y_k c_{v,k}$. The system pressure is evaluated using the ideal gas law given by $p = (\rho RT)/(\overline{W})$ where $\overline{W}$ is the mean molecular weight of the mixture.

As noted earlier, the simulations for the case of an RCEM involve a time-varying volume $V(t)$. Thus the specific volume v used in the energy equation can be expressed as $v(t) = V(t)/m$.

The volume profile $V(t)$ needs to be specified by the user to conduct the numerical simulations. This specification of the volume profile as a function of time is greatly simplified for this particular RCEM due to the encoder position feedback availability. The actual geometric volume, $V_g(t)$ can easily be computed from the encoder pulses.

3.2.2 Incorporating Heat Loss Effects

The experimental compression process and the subsequent constant volume conditions are not truly adiabatic in a real RCEM. One must account for the heat loss effects to accurately model the experiments. The following features in the experimental traces are indicative of the heat loss:

1. The measured pressures at EOC are lower than what an adiabatic system would produce

2. The post-compression heat loss is manifested as a slight droop in the recorded pressure values

These two non-ideal effects are modeled using separate approaches, as discussed below. The approach for heat loss modeling follows a procedure similar to that described in the previous work of Mittal and Sung [23].

3.2.2.1 Heat Loss and Dead Volume Effects During the Compression Stroke

An iterative procedure is used to incorporate an additional volume (V_{add}) into the true geometric volume at SOC such that the EOC pressures for the simulations match the experimental value. The volume specified in the simulations during the compression stroke is thus given by:

$$V(t) = V_g(t) + V_{add} \qquad (3.4)$$

The varying time volume of the reactor during the compression stroke $(0 < t < t_{EOC})$ thus consists of the instantaneous reactor volume $V_g(t)$ plus a positive empirical adjustment V_{add}. This procedure is illustrated graphically in Figure 3.1, where the correct starting geometrical volume for this specific case is $487\ cm^3$ (V_g at $t = 0$). This starting volume here needed to be increased by $14.25\ cm^3$ (V_{add}) to match the computed EOC pressure to the experimental value.
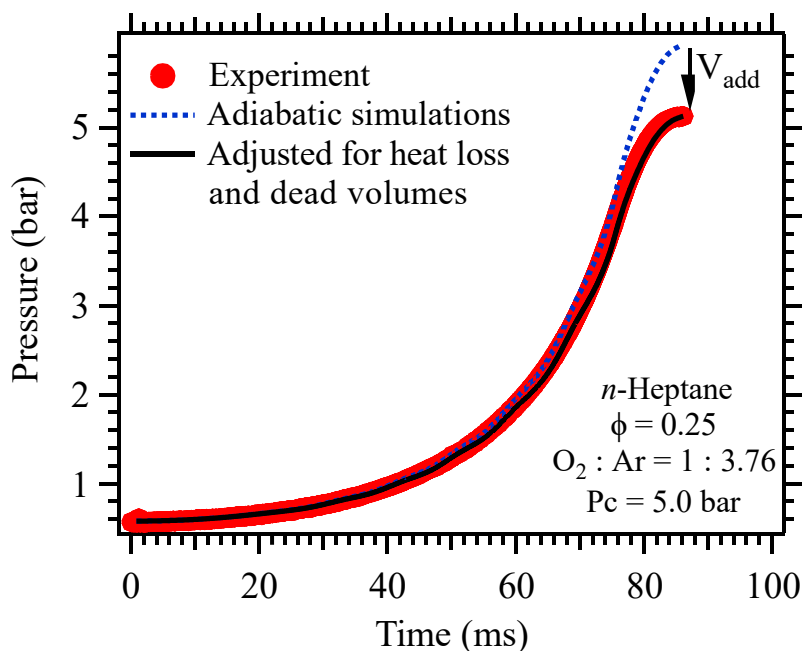
Figure 3.1: Modeling heat loss and dead volume effects between SOC and EOC.

3.2.2.2 Heat Loss Effects after the End of Compression

The post-compression pressure drops observed in the experiments are modeled by incorporating a fictitious time-varying volume expansion factor for the reactor volume after the EOC. Specifically, the volume at the end of compression is allowed to expand by a non-dimensional multiplication factor, $f(t)$, which is a function of time. This multiplicative volume expansion term is given by:

$$f(t) = 1 + \frac{\left(\dfrac{t - t_{EOC}}{a}\right)}{b + \left(\dfrac{t - t_{EOC}}{c}\right)^d} \; ; \; \forall \, t > t_{EOC} \tag{3.5}$$

The values for the four coefficients $[a, b, c, d]$ are chosen such that the post EOC pressure traces for both the experiment and simulation show matched pressure drop rates. The volume specified in the simulations during the post EOC duration is thus given by:

$$V(t) = \left[V_g(EOC) + V_{add}\right] \times f(t) \tag{3.6}$$
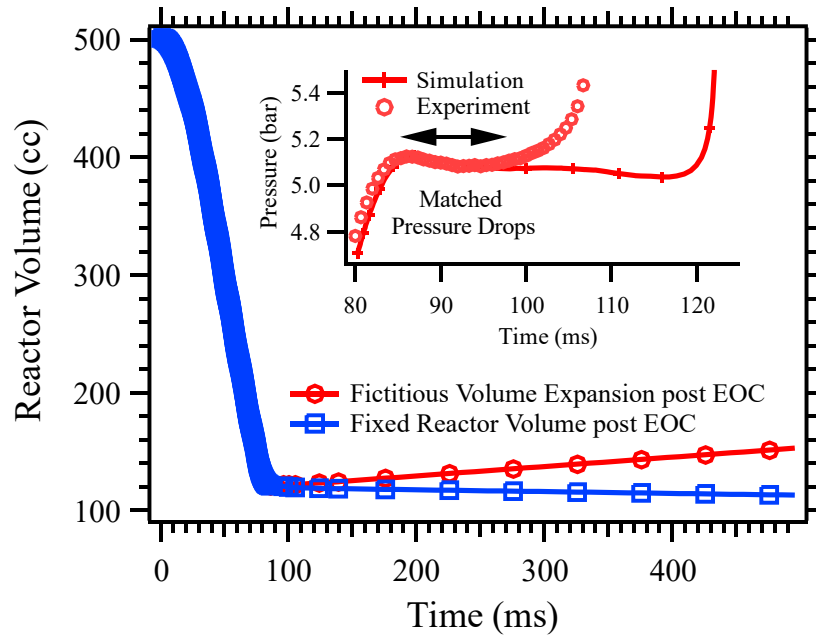
Figure 3.2: Modeling post EOC heat loss effects.

The approach is also similar to past studies using other rapid compression machines [23]. Figure 3.2 shows the effects of incorporating post-EOC heat loss into the model. It can be seen in the inset for Figure 3.2 that the inclusion of this fictitious volume expansion during the post-compression phase enables the simulated results to replicate a similar heat loss profile as in the experiments.

This approach does not explicitly model heat transfer via a heat transfer coefficient or wall heat flux. Instead, the non-ideal effects such as dead volume and wall heat loss are incorporated as relatively small fictitious adjustments to the reactor volume. The benefit of this approach is that it is relatively straightforward to simulate the system by merely specifying the apparent reactor volumes as follows:

$$V(t) = \begin{cases} V_g(t) + V_{add} & if \quad SOC < t \le EOC \\ [V_g(EOC) + V_{add}] \times f(t) & if \qquad t > EOC \end{cases} \tag{3.7}$$

As noted earlier, V_{add} and $f(t)$ are determined empirically while $V_g(t)$ is computed from the encoder pulse count during piston motion. A list of $(t, \ V(t))$ pairs is directly inputted to the simulation program as a CSV file along with the appropriate keyword indicating that a volume profile specification is being provided. The volume profile mentioned above is generated using a MATLAB® code whose output is the aforementioned CSV file. The simulation program's end-user uses the time-volume pair list, which already has the heat loss information contained within it. This method enables easy sharing of data in the form of a pre-specified volume profile without the need for implementing heat loss models.

3.3 Experimental Results for *n*-Heptane Autoignition

The autoignition of *n*-heptane was studied in the current RCEM over a temperature range of 600-763 K. The compressed pressures were between 3.0 to 6.5 bar. This first set of experiments demonstrates the machine's ability to operate in conventional mode with compression, followed by maintaining constant volume conditions after EOC. The experimental results for this set of trials consisted of a pressure trace (t, p) record. The ignition delay time was deduced from these experimental traces. The definition of ignition delay time was based on the position of peaks in the time derivative of the pressure $(t, dp/dt)$, as shown in Figure 3.3.
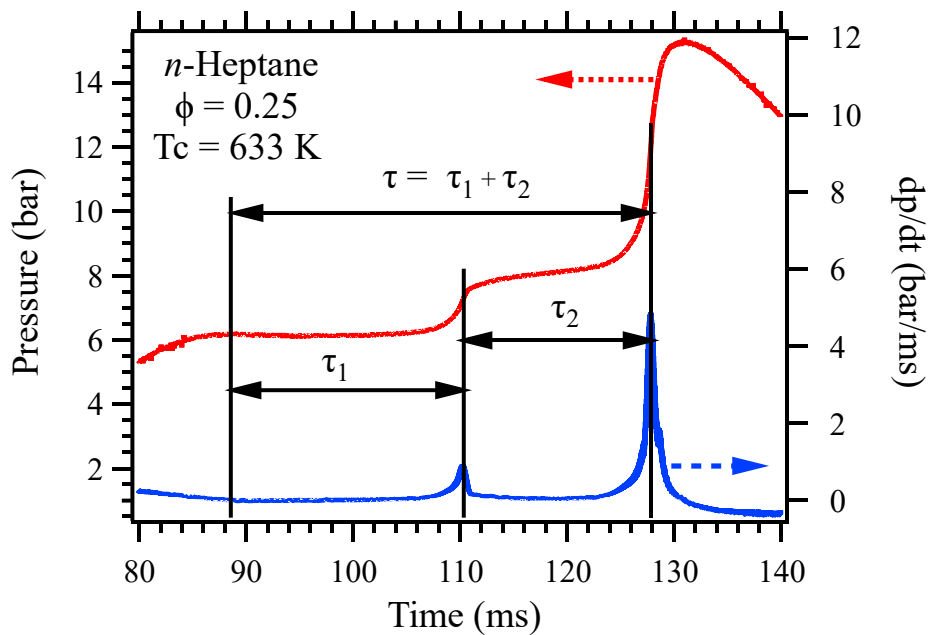
Figure 3.3: Definition of ignition delay

The first vertical solid line in the figure corresponds to the EOC and is taken as the reference time for measuring the ignition delay. The occurrence of the first peak in the time derivative (dp/dt) identifies the time corresponding to the first-stage ignition delay while the second peak corresponds to the hot ignition. The time difference between the EOC and the location of the first peak for the time derivative of pressure is the first-stage ignition delay time and is

designated as τ_1. The time interval between the first and second dp/dt peaks is the second-stage delay denoted by τ_2. The sum of the first-stage and second-stage delays corresponds to the overall ignition delay τ, i.e., the overall delay $\tau = \tau_1 + \tau_2$.

The test matrix for the *n*-heptane autoignition studies is summarized in Table 3.1. The experimental runs' initial temperature was 295.15 K for the test conditions. The oxidizer in the experiments consisted of oxygen and argon in the molar ratio of 1: 3.76.

Table 3.1: Test conditions

Equivalence Ratio ϕ	Compressed Pressure (bar)	Compressed Temperature Range (K)
0.20	5.5	720 – 763
0.25	5.0	600 – 745
0.35	5.0	592 – 617
0.50	3.0 & 4.0	604 – 717

3.3.1 Temperature Dependence of Ignition Delay

The experimental parameters impacting the ignition delay include the compressed temperature (T_c), the compressed pressure (P_c) and the equivalence ratio (ϕ). The compressed temperature, in particular, is the most important variable impacting the autoignition response. In general, an increase in the compressed temperature leads to higher reactivity. This increased reactivity of the system is manifested as a reduction in the ignition delay time. Large carbon number hydrocarbons do, however, tend to exhibit decreased reactivity with increasing temperature over a small temperature interval. This phenomenon is referred to as the negative temperature coefficient (NTC) of the reaction rate. This study conducted tests to verify and validate these known features for hydrocarbon oxidation in the low to intermediate temperature regime.
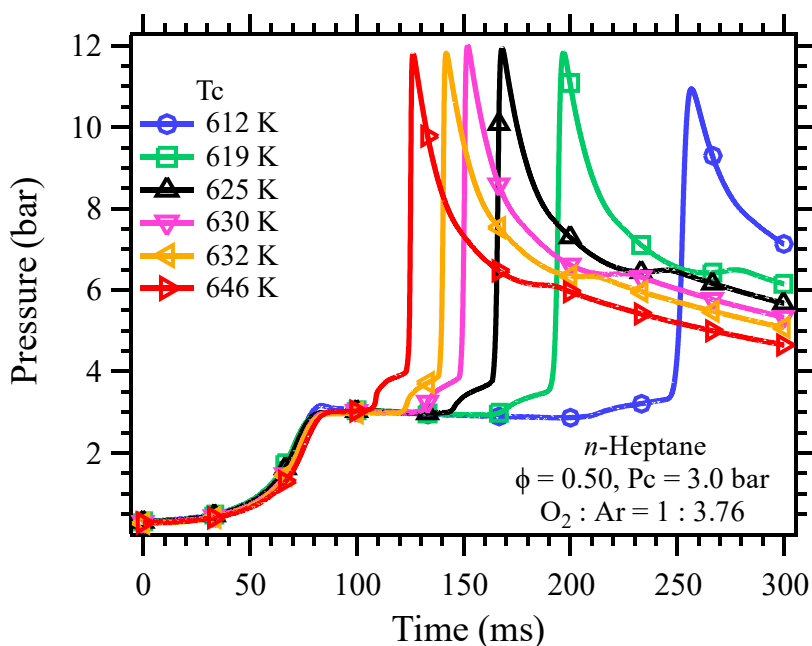
Figure 3.4: Pressure traces for n-heptane autoignition showing its dependence on the compressed temperature outside the NTC region

The experimental pressure traces shown in Figure 3.4 exhibit a strong two-stage ignition feature. Both the first-stage (τ_1) and overall ignition delays $(\tau = \tau_1 + \tau_2)$ decrease with

increasing temperature as one would normally expect. The second-stage delay (τ_2) is also found to decrease as the compressed temperature is increased. There is a rapid change in the relative ignition delay times in the low-temperature range (612-625 K) compared to the higher compressed temperature range (630-646 K), which is a typical Arrhenius dependence on temperature. The pressure traces in Figure 3.4 are consistent with all the known features of large carbon number hydrocarbon oxidation in the low-temperature range outside of the NTC. The pressure trace at the lowest temperature of 612 K demonstrates the ability of this machine to sustain reaction times as long as ¼ of a second without a significant drop in compressed pressure. This is partly achieved due to a large clearance volume at the end of compression (EOC), which tends to reduce the surface-to-volume ratio. A smaller surface-to-volume ratio leads to a lower fraction of the volumetric heat release being lost through the walls.
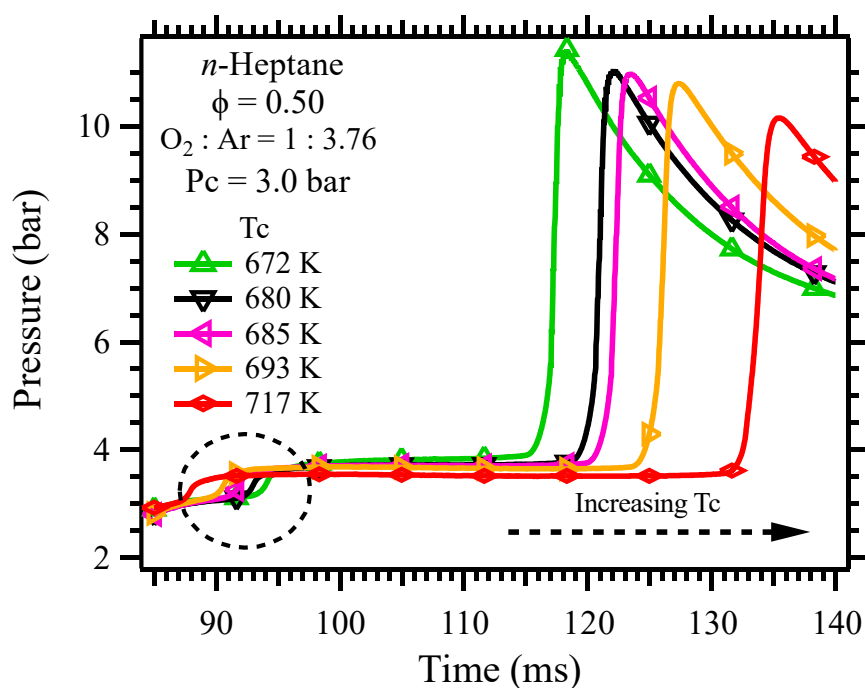
Figure 3.5: Pressure traces for n-heptane autoignition showing its dependence on the compressed temperature within the NTC region

The other important oxidation characteristic, namely the NTC effect, is shown in Figure 3.5, where the pressure traces show longer overall ignition delay times ($\tau = \tau_1 + \tau_2$) as the compressed temperature increases. This reduction in reactivity in the NTC region of the compressed temperature is also visible in the reduction of the peak pressure values with increasing temperature.

Interestingly, the trend for variation in first-stage ignition delay differs from that of the overall delay in the NTC region in that it continues to show a decrease with increasing temperature. This feature is encircled using dotted lines in Figure 3.5, and a zoomed-in view of the same is shown in Figure 3.6. The impact of reduced reactivity can still be seen in the form of reduced first-stage pressure rise with increasing temperature even though the first-stage delay continues to become smaller as the temperature increases.
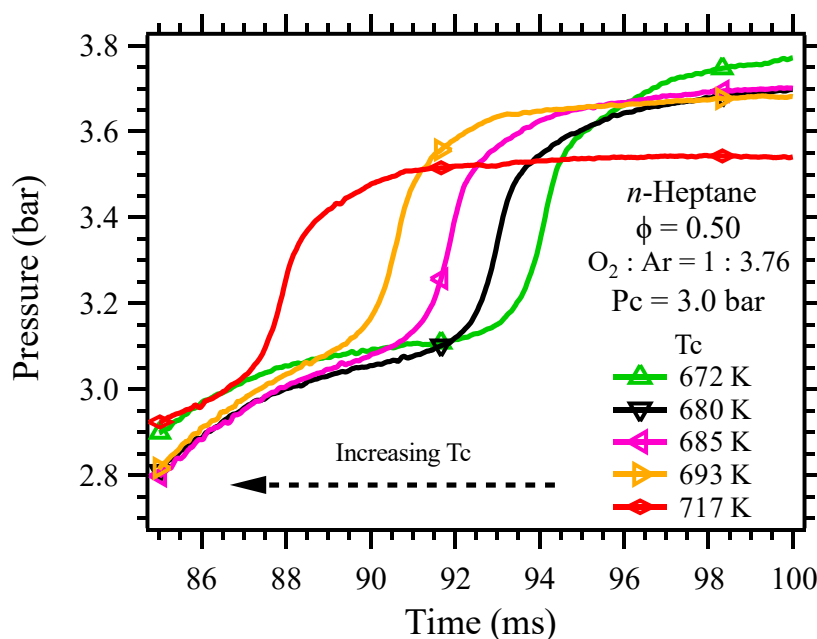
Figure 3.6: Pressure traces for n-heptane autoignition showing changes in the first-stage delay with varying temperatures.

A complete picture of the temperature dependence trends for *n*-heptane autoignition can be obtained by plotting the first-stage and overall ignition delay times against the inverse of compressed temperature as shown in Figure 3.7 (a) and (b). The plot for a pressure of 5 bar ($\phi = 0.25$) clearly shows that the overall ignition delay times initially show a rapid decrease with increasing temperature. This is followed by the NTC region, where the ignition delay time shows an increase with rising temperature. A further increase in temperature leads to an exit from the NTC region, and the ignition delay times go back to exhibiting a decreasing trend. A similar trend is also observed in Figure 3.7 (b) for a lower pressure of 3 bar. However, recovery from the NTC region is not apparent in Figure 3.7 (b) as this set of data does not cover as high a temperature range as that for Figure 3.7 (a).
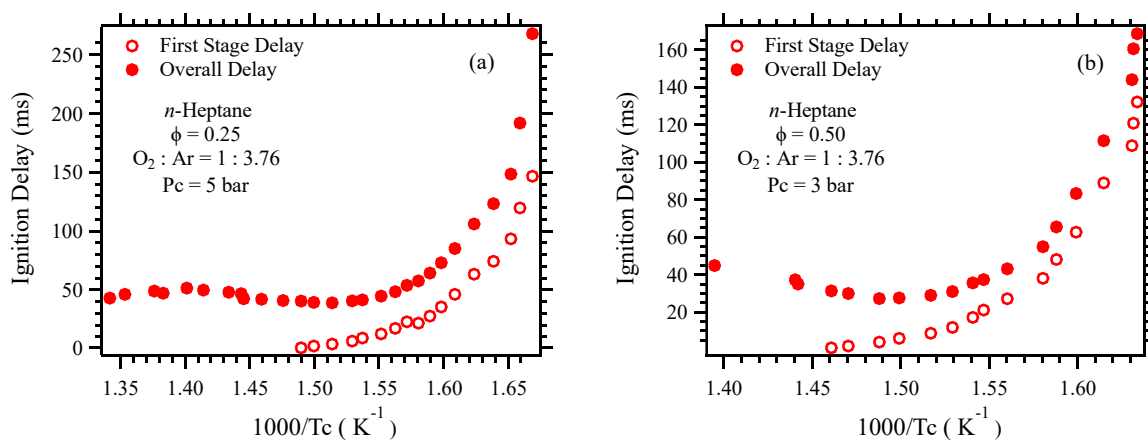
Figure 3.7: Temperature dependence of experimental ignition delay times

There is a reasonably good agreement for the temperature corresponding to the onset of the NTC region among both the data sets. On the other hand, the first-stage delay is found to exhibit a monotonically decreasing trend with increasing compressed temperature values. This dependence of the first-stage delay on temperature is separately plotted in Figure 3.8, where the two plots correspond to compressed pressures of 3 and 5 bar and for equivalence ratios of $\phi =$

0.5 and 0.25, respectively. The two datasets in Figure 3.8 show a very strong sensitivity of the first-stage delay to the compressed temperature, which is generally much stronger than the overall delay over the given test range.
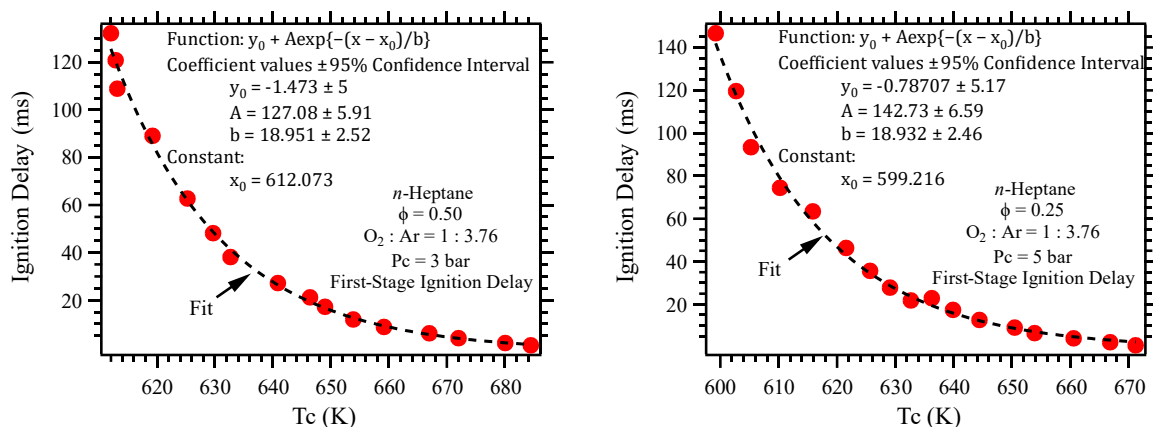
Figure 3.8: Fits to the experimental first-stage delay as a function of compressed temperature

The experimental data can be fitted as an exponentially decaying function of the temperature of the form $y = y_0 + Aexp\{-(x - x_0)/b\}$, where y is the first-stage ignition delay and x the compressed temperature. The quantities y_0, A, and b are coefficients of the fit with the appropriate units. The value for the offset constant $'x_0'$ is also determined as a part of the fitting process. The resulting fit is shown as a dotted line in the plot, and the coefficients and constants are provided along with their 95 % confidence interval estimates. Also, note that the 'offset' constant $'x_0'$ happens to be very close to the lowest temperature value present in the respective datasets. Similarly, the fitting constant A is close to the longest ignition delay time observed for the lowest temperature.

It is also noteworthy that the fits for these two cases having differing compressed pressures and equivalence ratios exhibit a near-identical slope given by the coefficient $'b'$ on a logarithmic scale for the ignition delay times. This implies that the first-stage delay is most responsive to

the compressed temperature changes and is not much impacted by differences in the equivalence ratio.

3.3.2 Influence of Equivalence Ratio on the Ignition Delay Time

The overall ignition delay time is also strongly influenced by the air to fuel ratio (A/F) of the reacting charge. This factor is customarily defined using the quantity termed as the equivalence ratio, which is given as $\phi = \frac{(A/F)_{st}}{(A/F)}$, where $(A/F)_{st}$ represents the stoichiometric mixture.
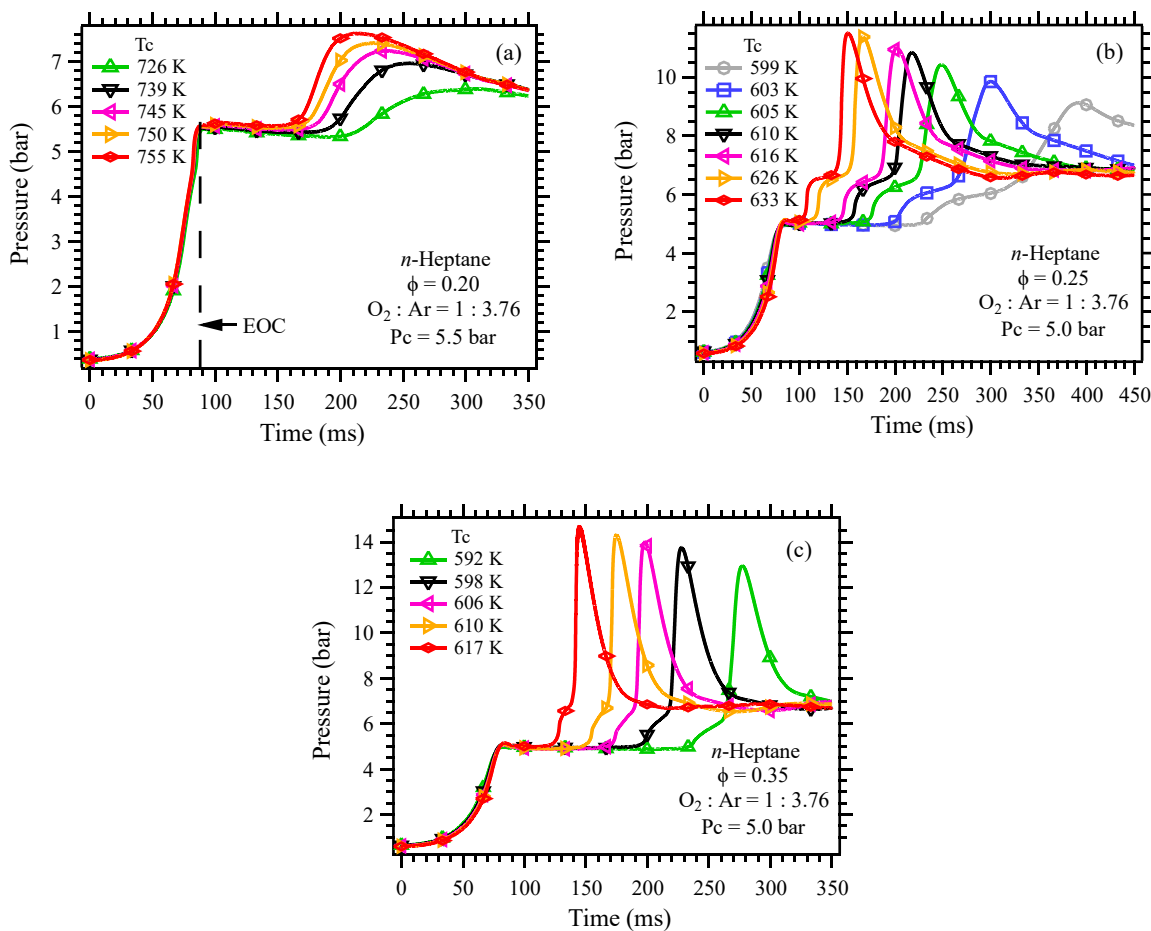
Figure 3.9: Pressure traces for n-heptane autoignition for various equivalence ratios at 5 bar

The plots in Figure 3.9 illustrate the dependence and impact of the equivalence ratio on the autoignition characteristics for a nearly constant compressed pressure. The most apparent feature evident in the pressure traces is that increasing the equivalence ratio leads to stronger combustion, as reflected in the successively higher peak pressures and pressure rise rates in

Figure 3.9 (a-c). Additionally, it is easier to ignite mixtures with a higher proportion of fuel (larger ϕ) at relatively lower temperatures for the conditions shown in the aforementioned figures.
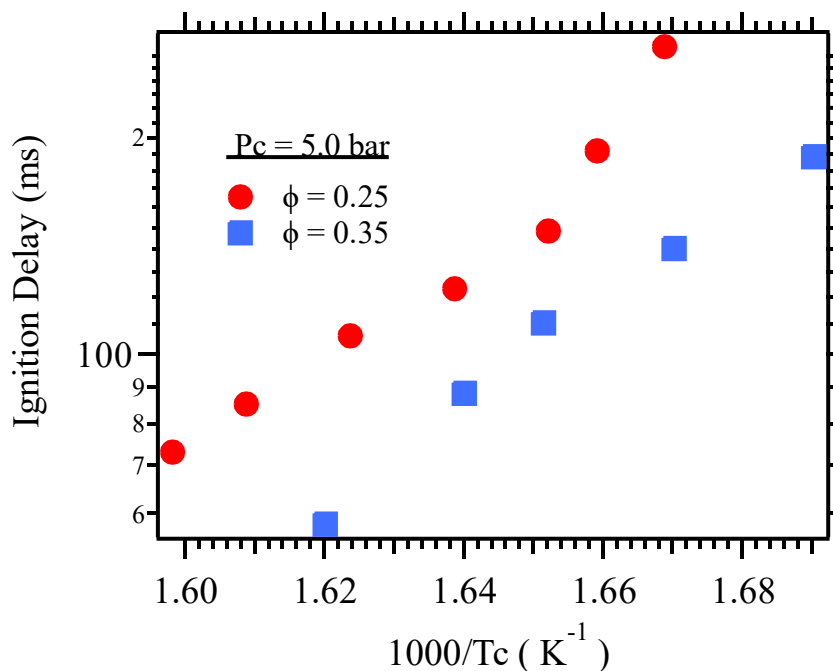
Figure 3.10: Overall ignition delay times for n-heptane at $\phi = 0.25$, $\phi = 0.35$ and 5 bar

The relative ability of mixtures with higher air to fuel ratio to autoignite quicker under similar compressed temperature and pressure conditions in the current set of experiments is shown in the plot of Figure 3.10. The ignition delay times for the leaner fuel-air mixture corresponding to an equivalence ratio of 0.25 are on an average 50% higher than those for an equivalence ratio of 0.35. The slopes of the respective plots are very similar for both the cases if one were to exclude the two data points with the largest ignition delay for the case of $\phi = 0.25$. The slight curvature for this case can be attributed to the greater heat loss due to long test times.

3.3.3 Effect of Compressed Pressure on Ignition Delay

The effect of pressure on the ignition delay times for *n*-heptane was also investigated in this work. Specifically, the compressed pressure was changed by adjusting the initial charge pressure and maintaining a fixed stroke length of 250 mm at a constant clearance. These experiments intended to demonstrate the machine's ability to resolve ignition delay differences even for relatively small increments of compressed pressure changes of 0.33 bar. The range of compressed pressure values covered in this test lie between 4.1-6.5 bar.
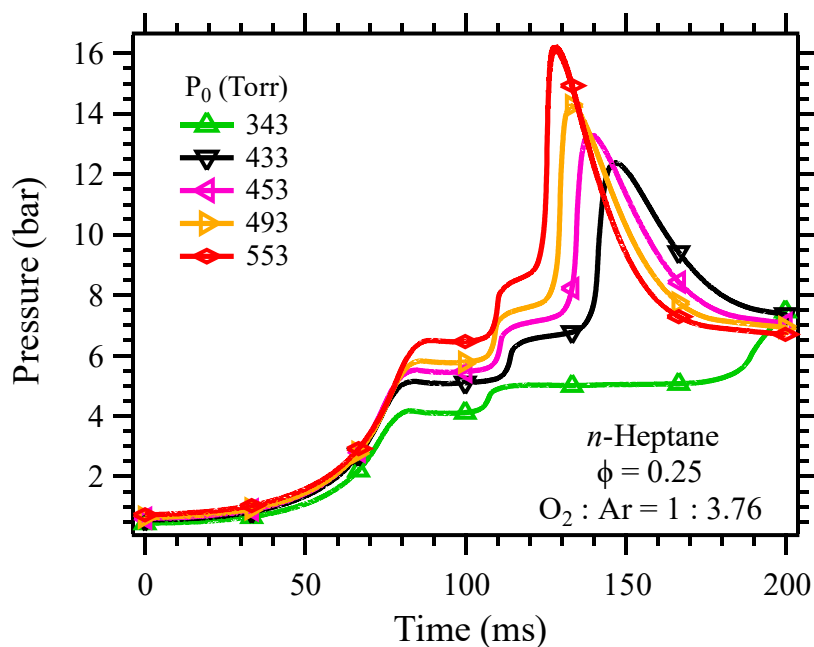
Figure 3.11: Pressure traces for varying initial pressure and a fixed stroke at $\phi = 0.25$.

Selected pressure traces corresponding to these experiments are shown in Figure 3.11. The traces show that while pressure variations significantly impact the overall and the second-stage delay, the first-stage delay appears to be relatively insensitive. As expected, high compressed pressures correlate well in a positive sense with a larger pressure first-stage pressure rise as well as the pressure gain during the hot combustion event.

The experimental ignition delay times inferred from the pressure traces are plotted as a function of the compressed pressure and shown in Figure 3.12. The reduction in overall ignition delay times with increasing pressure tends to follow a power-law trend for these test conditions. The fit, along with its associated coefficients, is also shown in the plot. The dotted lines are the confidence bands for the fit. It is somewhat surprising that the overall ignition delay times tend to show considerable sensitivity to pressure and change by a factor of approximately three over a 2.3 bar range interval. The ability to study the pressure sensitivity of the ignition delay is a useful tool for mechanism validation. This has been enabled by the long test times that can be achieved in this machine.
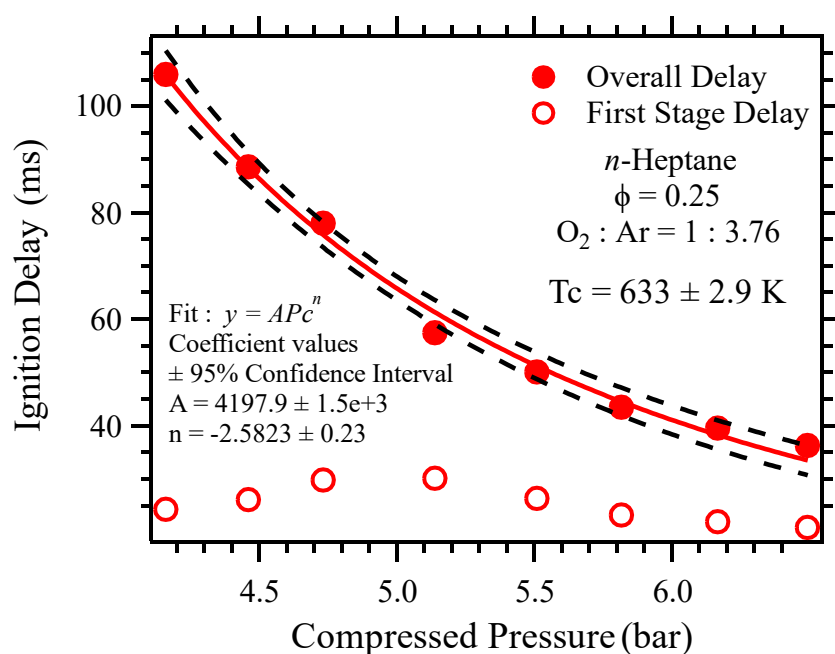
Figure 3.12: Dependence of ignition delay time on compressed pressure at $\phi = 0.25$.

The data for the first-stage ignition delay are also plotted alongside and appear as empty circles at the bottom of the figure. The first-stage delay does not show an appreciable change with variation in compressed pressure and is confined to a narrow region with an average value of 25.2 ± 3.4 milliseconds. It is difficult to discern a trend from the first-stage delay data in the plot, and further work is needed to understand its dependence on pressure.

3.4 Comparison of Experiments with Simulations

The data obtained in the experiments are compared to model predictions using a detailed chemical kinetic mechanism for the oxidation of *n*-heptane reported in the literature. As noted in the computational specifications section, it was obtained from the Lawrence Livermore National Laboratory and will hereafter be referred to as the LLNL mechanism [24-26]. All simulated results in the plots and discussions refer to this one mechanism used in this work. This mechanism is a result of continued efforts by several researchers in detailed mechanism development. This LLNL mechanism for *n*-heptane has been extensively validated against combustion data over a wide range of pressures and temperatures and includes low-temperature chemistry.

The ignition delay simulations reported in this work begin at the start of compression and incorporate non-ideal effects such as heat losses during and after the compression and prior to the ignition. The pure compression mode with the accompanying reactions is simulated. The determination of the various ignition delay times follows the same approach as for the experiments (*cf.* Figure 3.3). The comparisons are carried out for the overall ignition delay times as well as the first-stage ignition delay if it exists. Such comparisons are useful for assessing the predictive capability of chemical kinetic models for this global combustion marker, namely the ignition delay time. First, the complete pressure time histories for both the experiment and simulations are shown on a common plot. This is followed by a comparison of the inferred ignition delay times on another common plot. The temperature at the end of compression reported for the simulations is calculated based on the assumption of no reactions occurring before the end of compression. This estimation considers the correct mixture composition and

the temperature variation of specific heats for all the reactants. This procedure is further described in the appendices (section 7.1).

The plots in Figure 3.13 (a) and (b) are the simulated results at the lower and higher end of the compressed temperature range, respectively. In general, the simulations predict a slightly lower overall ignition delay than the experiments, i.e., the model is comparatively more reactive.

At the temperature of 603 K shown in Figure 3.13 (a), the simulated onset of first-stage pressure rise occurs slightly earlier but reasonably close to the experiments. The second-stage delay for the simulations is significantly short, resulting in a shorter overall delay than the experiments. The first-stage pressure rise is also well predicted. For the next set of traces corresponding to 632 K, the overall delays are in excellent agreement. However, the simulated first-stage delay is somewhat longer.
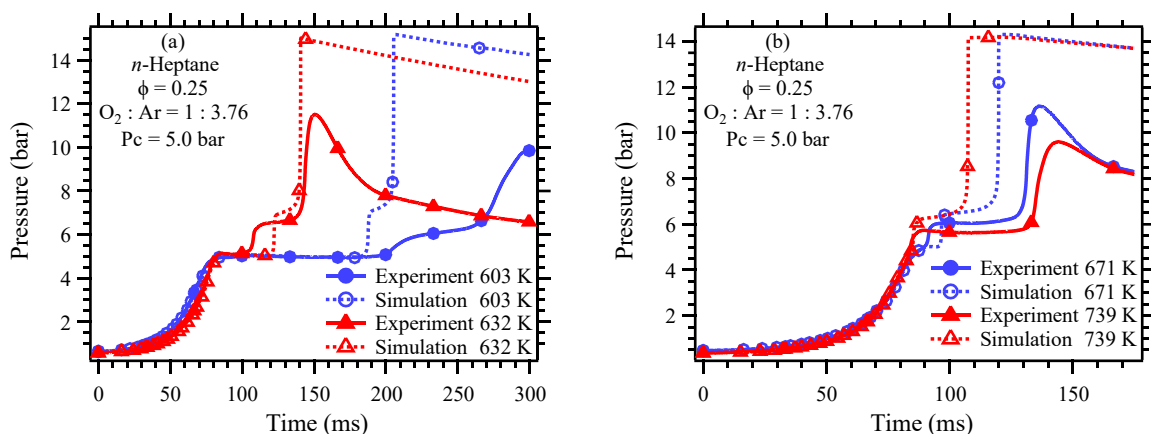
Figure 3.13: Comparison of experimental and computed pressure traces at $\phi = 0.25$ and 5 bar

The results for higher compressed temperatures are shown in Figure 3.13 (b). For this case, the experiments are within the region of NTC, i.e., higher compressed temperatures lead to longer delays with $\tau(739\ K) > \tau(671\ K)$. The simulations in this region cannot capture this feature, and the simulated results for this temperature range continue to predict shorter ignition delays

as the compressed temperature increases. A comprehensive overview of the performance of the mechanism over the entire temperature range covering all the experimental data points can be seen in the plot shown in Figure 3.14. The individual data points in this figure are the overall ignition delays which were inferred from corresponding pressure traces. The plot shows that there are three distinct regions that one must consider to evaluate the model performance. The first region is in the lowest temperature range of 600-625 K in the right sixth of the plot, where the computed ignition delays shown as empty symbols are lower compared to the experiments. The next region in the temperature range of 630-670 K is where the computed and experimental results are in excellent agreement. Finally, for temperatures between 675-745 K, the computed results slowly diverge from the observed experimental values and are lesser in value.
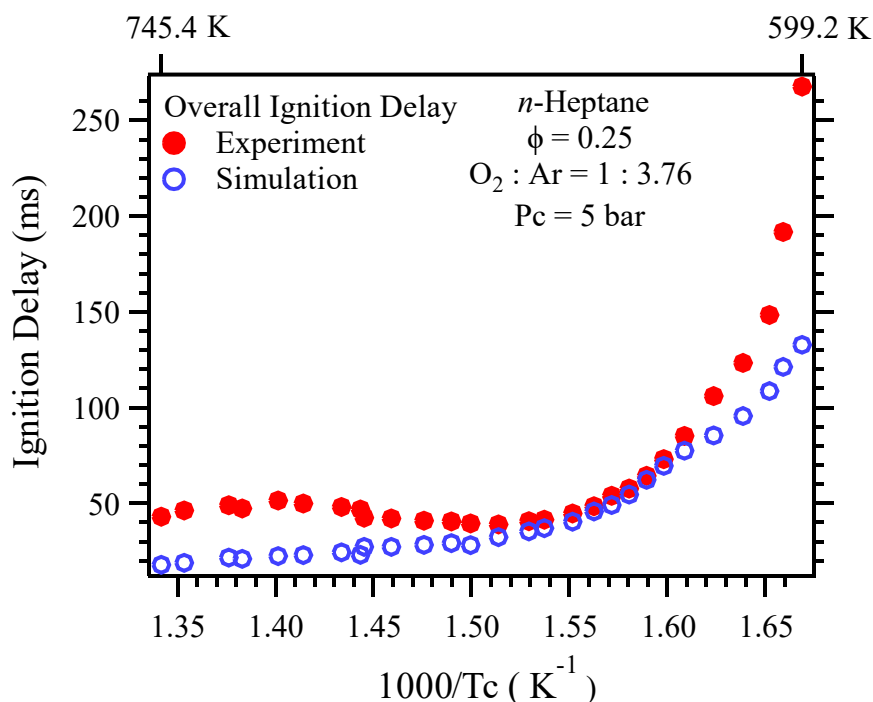
Figure 3.14: Comparison of experimental and computed overall ignition delay times at $\phi = 0.25$ and 5 bar

The apparent reason for the mismatch in predicted and actual values in the 675-745 K range is that experiments begin to show an NTC behavior. Simultaneously, the computations continue to predict a monotonic decrease of ignition delay with increasing temperature in that region.

Computed values for the first-stage ignition delay times correctly predict the monotonic decrease in experimentally observed values with increasing temperature. There is a reasonable agreement between the two over the entire test temperature range. The experimental first-stage delays are slightly shorter than the computed values except for the three lowest temperature test conditions for ignition delay times close to and above 100 ms.
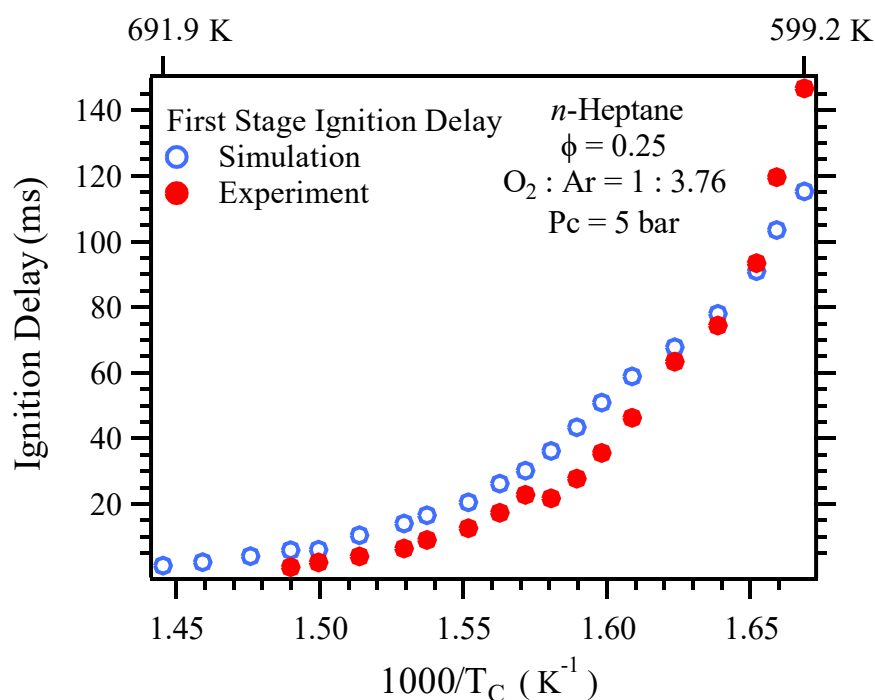
Figure 3.15: Comparison of experimental and computed first-stage ignition delay times at $\phi = 0.25$ and 5 bar.

The higher reactivity of the chemical kinetic model carries over to slightly richer fuel-air mixtures for an equivalence ratio of 0.5 and for a slightly lower pressure of 3.0 bar. A comparison of the results under these conditions is shown in Figure 3.16, where both the first-

stage and the overall simulated ignition delay times are shorter than the experiments. This figure also demonstrates two important features of this rapid compression expansion machine. First, this device is capable of accessing pressures as low as 3 bar without any indication of vibrations. Typical mechanically stopped RCM's generally have difficulty operating in the low-pressure range due to excessive machine vibrations. Second, it is possible to obtain exceptionally long test times in the current device. The experimental results for 612 K in Figure 3.16 have an overall ignition delay of one-quarter of a second. Even more impressive is the machine's ability to maintain the compressed pressure for such a long interval, demonstrating that the heat losses are negligible under these test conditions.
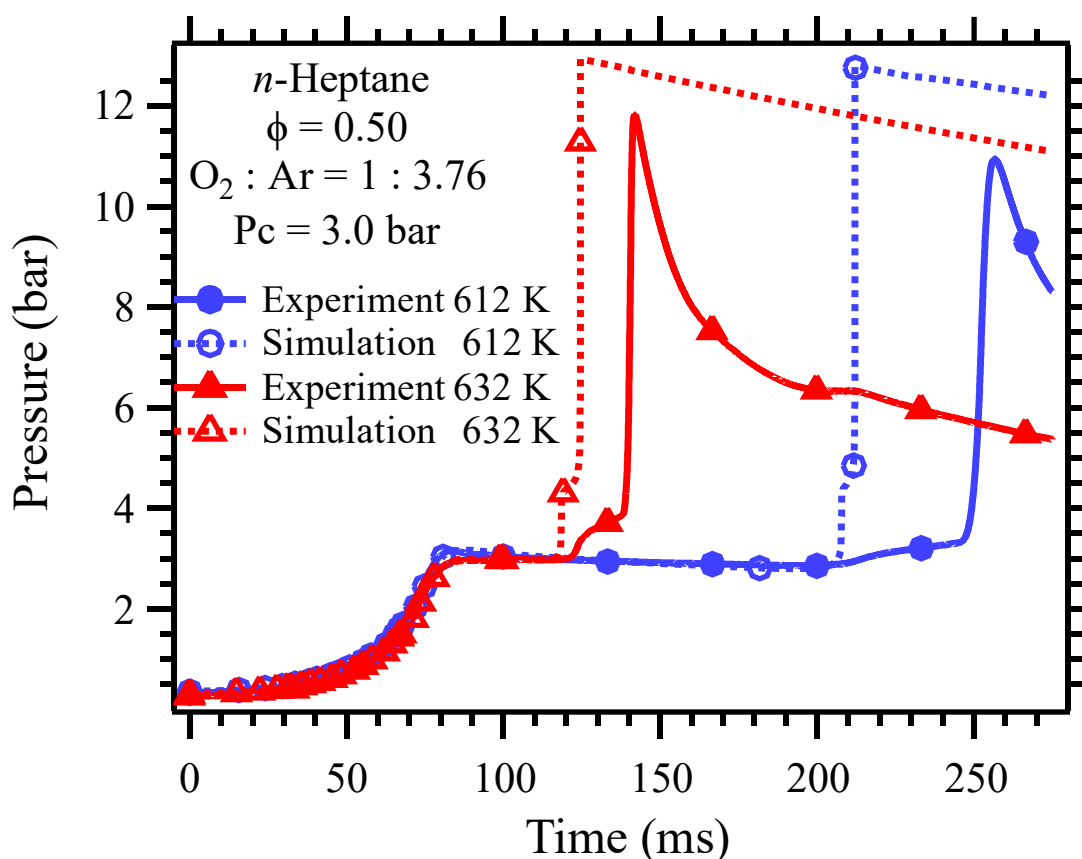
Figure 3.16: Comparison of experimental and computed pressure traces at $\phi = 0.50$ and 3 bar

3.5 Conclusion

The ignition delay times for *n*-heptane oxidizer mixtures under high pressure and low-to-intermediate temperature conditions were obtained using a rapid compression expansion machine. The experiments were designed to demonstrate the machine's capabilities for observing critical characteristics related to the hydrocarbon autoignition process, such as the two-stage ignition phenomenon and the existence of a negative temperature coefficient region for the reaction rate. The experimental results also yielded the temperature and equivalence ratio dependence of the ignition delay time. An exponential dependence of the ignition delay times on compressed temperature was found. The slope of the fit exhibited minimal dependence on pressure and equivalence ratio. The effect of pressure variation on the ignition delay times over the 4.1–6.5 bar range was also obtained, and it showed an inverse dependence with a pressure exponent of approximately negative 5/2. The experimental results were also compared to simulated results obtained using a detailed kinetic mechanism. The comparison shows the kinetic model to be slightly more reactive than the experiments with a good agreement in terms of the trend for temperature variation of the ignition delay times. Among the most interesting findings of this part of the research was obtaining substantially long ignition delay times than what has been previously possible. This work measured ignition delay times over 0.25 seconds at around 3 bar. Typical RCM results are in the range of 50 ms or lower for their respective lower operation limits. This has been made possible by this machine's ability to work at lower pressures without vibrations, along with the significantly reduced heat loss as manifested by the post-compression pressure drop.

.

4 Stable Intermediate Speciation during *n*-Heptane Autoignition in an RCEM

4.1 Introduction

A significant contribution of this study to the understanding of *n*-heptane oxidation kinetics is through time-resolved speciation studies. The ability to quantify the time evolution of pre-ignition stable intermediates adds a robust target for the validation of kinetic models than global responses such as ignition delay times. In the past, such studies have been limited to low-pressure conditions using apparatuses such as closed vessels [50]. The rapidity of combustion reactions has been a significant hurdle for conducting speciation studies under high-pressure conditions. This difficulty is evident from the chronological review of such product distribution studies from 1976 to 1995 provided in the work of Griffiths and Mohamed [51]. They document a total of 80 such studies with only five studies above atmospheric pressure conditions and just two RCM studies. Most of the studies tracking product evolution as a function of time are limited to sub-atmospheric conditions in closed vessels. The lack of RCM speciation data can be explained by the fact that researchers employed the diaphragm rupturing technique, which is tedious, requires machine disassembly and often lacks repeatability. The current RCEM can provide reliable data with relative ease on the reactivity build up during the ignition chain reaction sequence. The data provided is in the form of stable species evolved during the ignition process at various times.

It is of great interest to examine the product distribution during the induction as well as the acceleratory period of the ignition process. This would, however, require quenching the reactions during these phases of the chain reaction sequence. The current RCEM can easily accomplish this in a very repeatable and programmable fashion.

4.2 Quenching Reactive Mixtures

An example of the reaction's quenching during the second-stage induction period and the following acceleratory phase is shown in Figure 4.1. The quench is very rapid, and the process is very repeatable, as seen from the overlap of the two curves in the figure. Operating the RCEM in rapid compression expansion mode allows for speciation studies to be conducted. The time delay between the end of compression and the piston retraction can be varied in a controlled fashion. The quick expansion leads to the quenching of the reactive mixture. Quenching of the reactive mixture freezes the oxidation process at different times during the induction period. The quenched products can be used for qualitative and quantitative analysis using a GC-MS and other analytical tools.
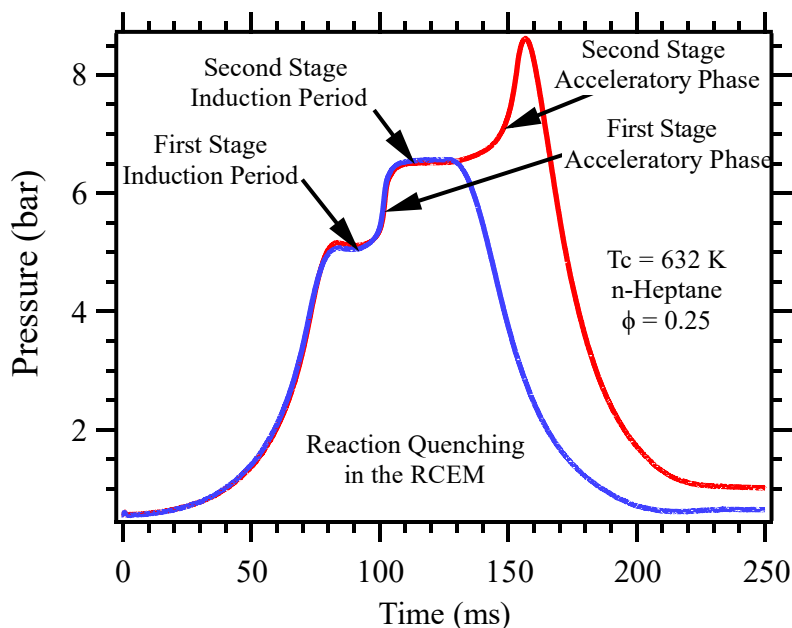
Figure 4.1: Rapid compression expansion pressure trace definitions.

Quenching of reactions during the second induction period is shown in Figure 4.1. The red line at the top is a typical pressure trace of an experimental run allowed to progress towards second-stage ignition. In contrast, the blue line is the pressure trace of an experimental run quenched

before second-stage ignition begins but after the first-stage ignition has occurred. These experiments were conducted at $\phi = 0.25$, $P_c = 5$ bar, $T_c = 632$ K, and $O_2 : Ar = 1 : 3.76$ molar ratio. This study examines the product distribution in six different samples where the quench was initiated at times corresponding to 105.6, 115.6, 125.6, 135.6, 145.6, and 155.6 milliseconds. Note that while the products are examined for quench initiation time in programmed increments of 10 milliseconds in this work, it is possible to do so experimentally in increments as low as 0.5 milliseconds, if needed.

This capability of precisely timed and programmatically controlled quench is unique to this machine.

The quench experiments with a high timing precision coupled to the availability of pressure and reactor position information open up an entirely new type of validation target for kinetic models. One can now accurately simulate the piston motion trajectory, including the expansion stroke, with the inclusion of detailed kinetics to compare the changes in stable end product composition during various pre-ignition stages.

Examples of comparative experimental and simulated pressure traces are shown in Figure 4.2. The simulated results shown in the figure as solid blue lines have been obtained for identical initial conditions and the same reactor volume profile as for the experiments. The figures show that although the volume profiles are similar, the system evolution is quite different between the experiment and the simulation. At the first quench time of 105.6 ms, the first-stage ignition has set in for the experiment, while the simulation has yet to exhibit the first-stage reactivity. The two other quench times of 115.6 and 125.6 ms show that both the experiment and simulation have undergone the first-stage ignition and are within the region of second-stage delay, and the second-stage ignition has not yet set in. It is interesting to note that the magnitude

of the first-stage pressure rise for both the experiments and the simulations is quite similar. At the quench time of 145.6 ms, the computed case has already undergone the second-stage (hot) ignition, while the experimental case is just at its onset for the same. These trends indicate that the mechanism is slightly slower in predicting the onset of the first-stage reactivity in that it has a longer first-stage delay compared to the experiments for all cases under consideration in Figure 4.2. On the other hand, the computed trace has a much smaller second-stage delay, leading to an overall delay shorter than the experiments.

It is possible to follow stable intermediates' evolution by collecting samples corresponding to the shown quench times and analyzing them quantitatively using a gas chromatograph-mass spectrometer system. As a first approximation, for the computations, one can assume that the reactions freeze instantly at the start of the quench. Under this assumption, and noting that each of the six quench experiments corresponds to identical initial conditions, one can obtain the computed species evolved from a single simulated case. This simulated case then corresponds to the one with the longest quench time (155.6 ms), and we can use the information on species evolution at other shorter times.
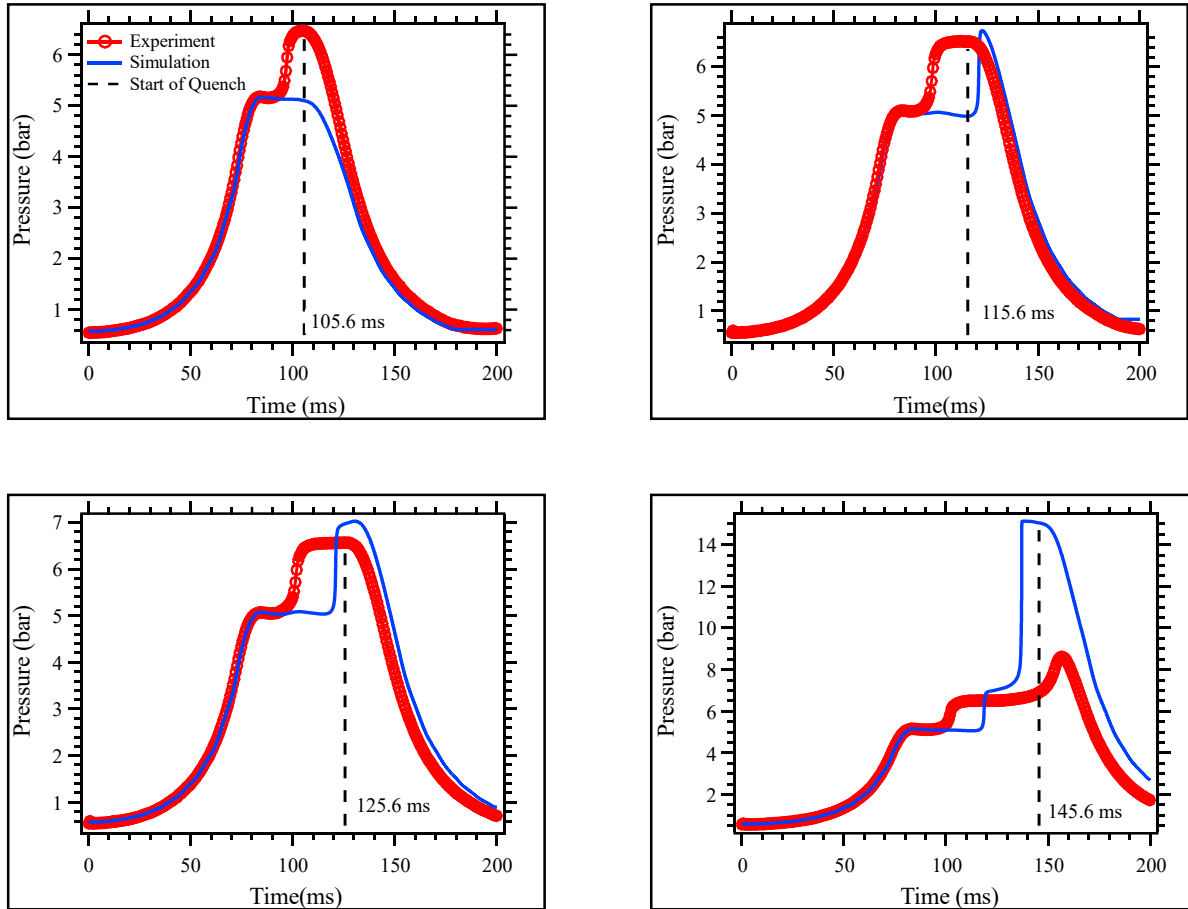
Figure 4.2: Selected rapid compression expansion pressure traces comparing experiments to simulated results

An alternative and possibly more rigorous approach would be to follow each computation right up to the end of the expansion stroke, i.e., each case needs to be simulated individually, as shown in Figure 4.2. The stable intermediate product distribution is then compared for both the experiments and computations at the same time towards the end of the expansion stroke. The two approaches are discussed in sections 4.3 and 4.4, respectively.

4.3   Time Evolution of Stable Intermediates

Stable intermediary speciation studies were carried out by interrupting the evolution of the ignition process utilizing rapid quenching. The speciation study was done for *n*-heptane fuel and followed the set of experiments that measured ignition delay times. The ignition delay experiments were used to identify operating conditions most suitable for quenching. After determining a proper compression ratio, the reactions were quenched by rapid expansion in successively increasing time intervals of 10 milliseconds over six different runs.

A GC-MS system comprising a Trace GC Ultra and a Trace Dual-stage Quadrupole Mass Spectrometer was used for species analysis. The quenched sample collected after each experiment was run through a 1ml gas sample loop connected to the GC-MS system. A 50-meter fused silica capillary column (Rtx-DHA) was used for the separation of the compounds. This column is suitable for light hydrocarbons as well as polar oxygenates. It was observed that the low carbon number oxygenates and C_2 compounds tend to elute very early and had overlapping peaks. This work quantifies selected C_2-C_5 alkenes, aldehydes, ketones, and oxygenates present in the total ion chromatogram using the peak area method. The data provided is in the form of stable species concentrations present during the ignition process at various times. An example of the speciation data during the first-stage induction period is shown in Figure 4.3. The plot shows the total ion chromatogram obtained by separating the quenched gas constituents using a gas-chromatograph and identified using a mass spectrometer. At least 26 intermediate species were detected under the conditions shown in Figure 4.1.
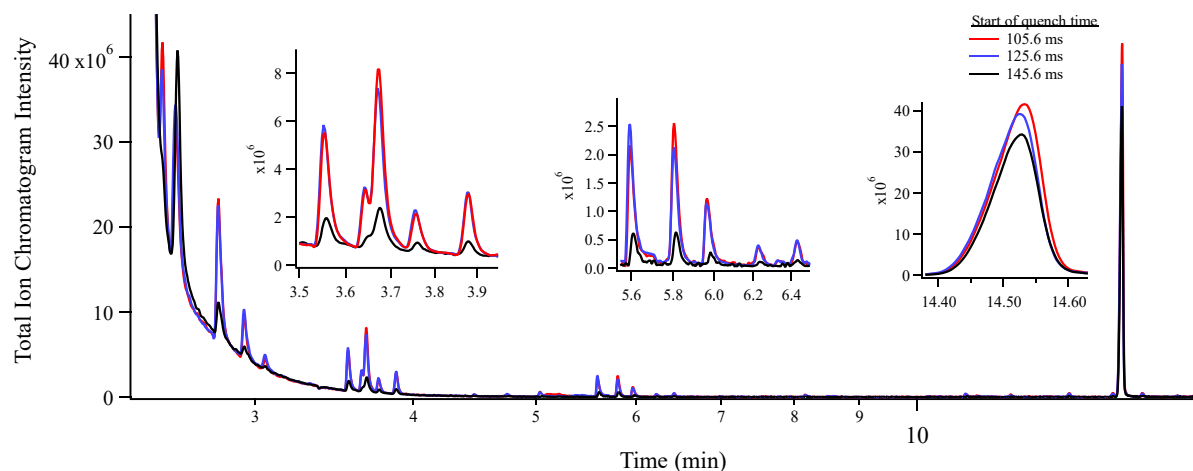
Figure 4.3: Chromatogram of stable intermediates

4.3.1 Qualitative Analysis of Quenched Products

A qualitative analysis of the quenched products was carried out based on the peaks in the total ion chromatogram. The NIST mass spectral library was used for species identification [52]. Determination of retention time for each peak and its identification was carried out using an automated processing method applied to all chromatograms. For a given retention time, the qualitative analysis routine returned multiple possibilities for the identity of a species with an associated probability. The species with the highest probability was selected to be reported in this analysis. The list of species, their retention time, molecular formula, and the probability of identification are provided in Table 4.1. The data in the table is for the shortest quench time of 105.6 ms. The identity of the species remained the same across all other test conditions, with variations being observed in the probability and the peak height.

Table 4.1: List of species identified in the GC-MS analysis (ϕ = 0.25, P_c = 5 bar, T_c = 632 K, and $O_2 : Ar$ = 1 : 3.76)

	RT	Compound Name	Molecular Formula	Molecular Weight	Probability %
1	2.6	Propene(Propylene)	C3H6	42	52
2	2.81	Acetaldehyde	C2H4O	44	83
3	2.94	**2-Butene**	C4H8	56	80
4	3.06	Ethylene oxide	C2H4O	44	23
5	3.16	2,5-Furandione, dihydro-3-methylene-	C5H4O3	112	29
6	3.32	Methyl ether	C2H6O	46	95
7	3.56	2-Propenal	C3H4O	56	96
8	3.64	**Acetone**	C3H6O	58	82
9	3.67	**Propanal**	C3H6O	58	76
10	3.76	**Propylene oxide**	C3H6O	58	64
11	3.88	**1-Pentene**	C5H10	70	43
12	4.48	Isoprene	C5H8	68	46
13	4.75	2-Propen-1-ol	C3H6O	58	63
14	5.04	1,3,5-Trioxane	C3H6O3	90	59
15	5.11	3,4-Epoxy-2-Hexanone	C6H10O2	114	27
16	5.21	Hexane, 2,4-dimethyl-	C8H18	114	29
17	5.6	Methyl vinyl ketone	C4H6O	70	92
18	5.81	**Butanal**	C4H8O	72	84
19	5.97	**2-Butanone**	C4H8O	72	92
20	6.23	**Oxirane, ethyl-**	C4H8O	72	76
21	6.43	**1-Hexene**	C6H12	84	61
22	8.16	2-Butenal	C4H10O	70	54
23	10.93	1-Penten-3-One (Ethyl Vinyl Ketone)	C5H8O	84	55
24	11.16	Pentanone-2	C5H10O	86	24
25	11.87	**Pentanal**	C5H10O	86	30
26	13.2	1-Heptene	C7H14	98	69
27	14.53	**n-Heptane**	C7H16	100	78

A total of eleven species were selected from the list of identified species for quantitative analysis and are shown in boldface in Table 4.1. The comparison of quantitative experimental and numerical results is provided in section 4.3.2. The species identified in this study include alkenes, aldehydes, ketones, and ethers.

It is well recognized that the oxidation of hydrocarbons proceeds via a chain mechanism. The steps involved are [53] :

$$RH + O_2 \rightarrow R^* + HO_2 \qquad R^* + O_2 \rightarrow RO_2^* \qquad RO_2^* + RH \rightarrow ROOH + R^*$$
$$(initiation) \qquad\qquad (propagation) \qquad\qquad (propagation)$$
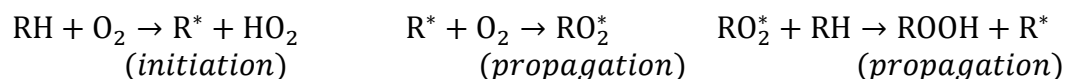
In addition to the straight and branched chain, they also include the so-called degenerate chain branching mechanism between 500-900 K.

$$ROOH \rightarrow RO^* + OH^*$$

The degenerate branching reactions act as secondary initiations and involve the relatively stable product of the primary initiations and not the parent fuel itself [54, 55]. This imparts several unique characteristics such as cool flames and the negative temperature coefficient behavior of ignition delay to gas-phase combustion of hydrocarbons. The onset of the first-stage ignition and the consequent first-stage delay (τ_1) is one manifestation of such behavior. The branched-chain reactions are also associated with an induction period. This is characterized by a time interval during which there is no pressure rise observed in the pressure traces after compression. The induction period depends on the net branching factor Φ [56]. The induction period is followed by a period of acceleratory autocatalysis attributable to the decomposition reactions of the type $ROOH \rightarrow RO^* + OH^*$ involving hydroperoxide species for large carbon number hydrocarbons [53]. The time variation of the products during this period can be shown to be related to the net branching rate Φ. It can be shown that $d\Delta(products)/dt = \Phi\Delta(products)$ or $ln\Delta(products) = \Phi t + constant$ [56]. The experiments are thus potentially capable of

elucidating the relationship between the change in an intermediate product formation rate and the branching factor during various stages of ignition.

The time evolution of a few selected species is shown in Figure 4.4 and Figure 4.5. The plots show the stable intermediate species evolution trend as the ignition process proceeds through the second-stage induction and ignition steps.

RT	Species
3.55	2-Propenal
3.64	Acetone
3.67	Propanal
3.76	Propylene Oxide
3.88	1-Pentene
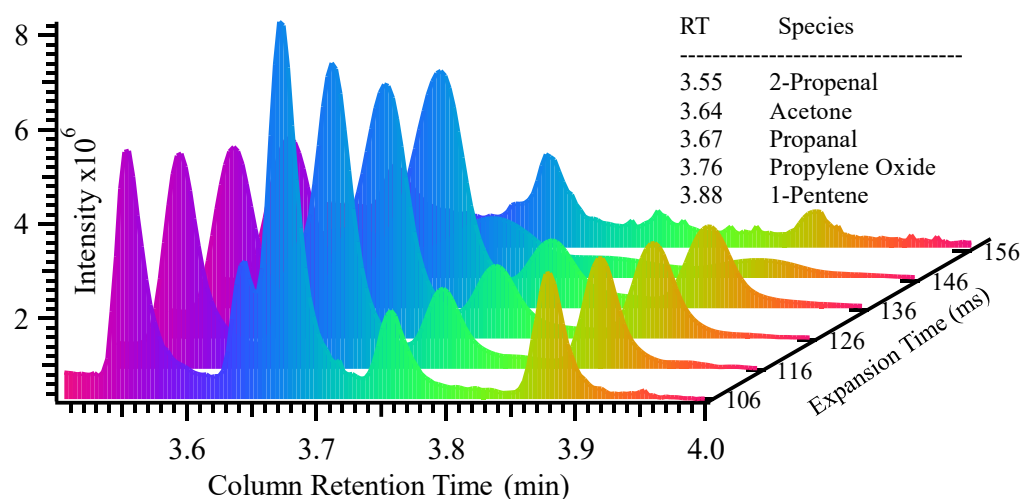
Figure 4.4: Total ion chromatograms with expansion times. RT of 3–4 min.

The first plot in Figure 4.4 shows the lighter compounds present in the quenched products that elute from the GC column between 3.0 and 4.0 minutes. The horizontal and vertical axis of the plot represents the GC column retention time and the MS signal Intensity, respectively. The third axis represents the six quench initiation times in the speciation experiments. Note how the maximum area under the peak for the propylene oxide, a cyclic ether, occurs later compared to other compounds.

RT	Species
5.81	Butanal
5.97	2-Butanone
6.23	Oxirane, ethyl-
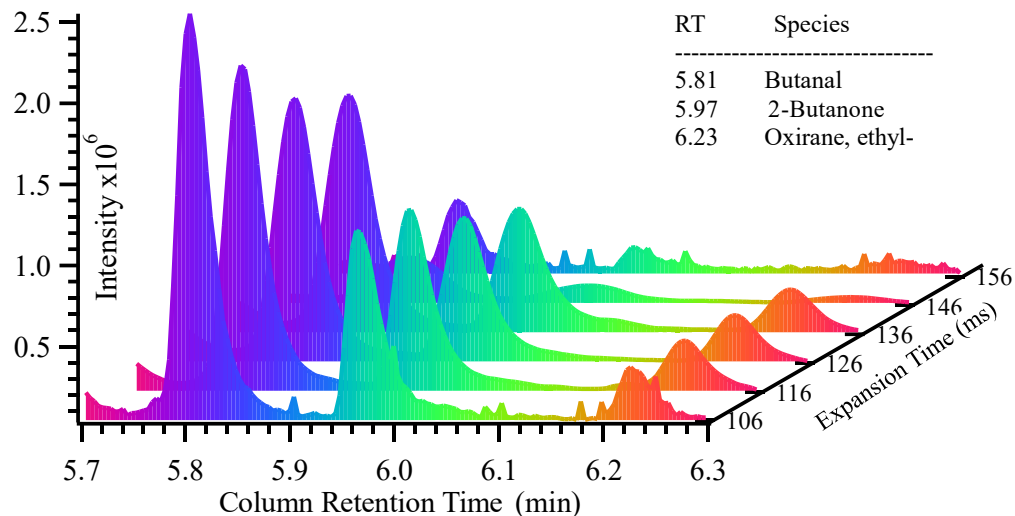
Figure 4.5: Total ion chromatograms with expansion times. RT of 5.7–6.3.

The next set of relatively heavier compounds eluting between 5.7 and 6.3 minutes are shown in Figure 4.5. Again, similar to the previous plot, the aldehyde is the most abundant component. Another interesting feature is that the peak aldehyde concentration occurs at the earliest quench time of 105.6 ms while the ketone and cyclic ether peak at a slightly longer quench time. These plots provide a straightforward visual interpretation of the relative abundances and time evolution of the stable intermediates.

4.3.2   Quantitation of Selected Intermediate Species

A total of eleven stable intermediate species were chosen to determine their concentrations during the various stages of system evolution between the first and second stages of ignition. The peak area method was used to obtain the species concentrations in conjunction with individual calibration curves for each of the eleven pure compounds. An external standard method was developed which used known concentrations of pure components. The calibration gas samples were prepared using the method of partial pressures in the mixing chamber described previously. Note that the pure components were available in the liquid form and were injected into the mixing chamber while ensuring that their respective partial pressures in the mixture were lesser than their vapor pressure at the mixture temperature. The chosen pure components span a wide range of chemical classes that include alkenes, carbonyl compounds (aldehydes and ketones), ethers, and alcohols. These standards were run in the GC-MS under similar conditions as the sample. A linear calibration curve was fit to the peak areas versus the known concentrations for a given compound.

An example of the area under a pentene calibration standard with a specified value of 67 ppm is shown in Figure 4.6. The calculated area of the curve for this case is 8,697,979 units. Seven such calibration standards with varying pentene concentrations were run through the GC-MS, and the resultant linear fit of the respective areas versus the concentrations are shown in Figure 4.7. Note that the fitting procedure forces the line through the origin, i.e., one assumes that the area is zero for a concentration value of zero.
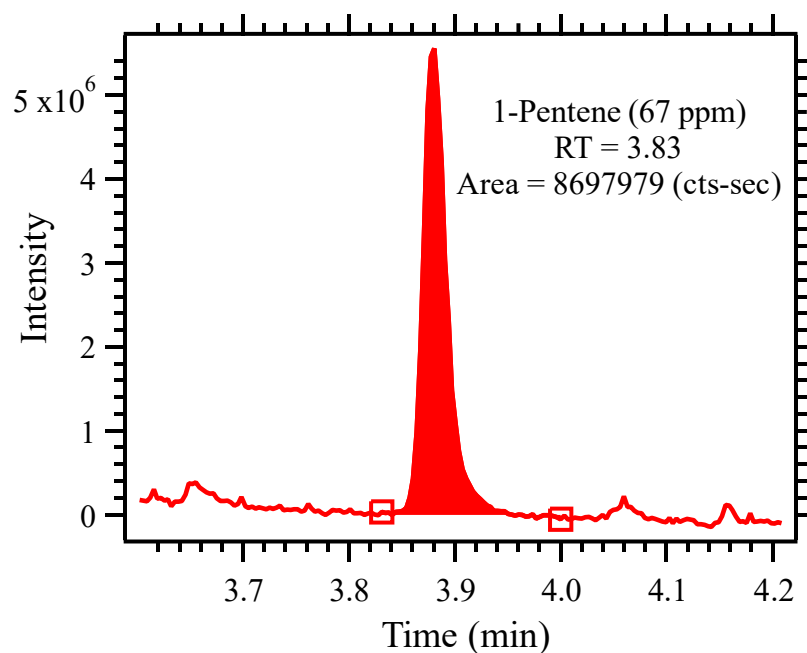
Figure 4.6: Limits of integration for a 1-pentene calibration standard of 67 ppm
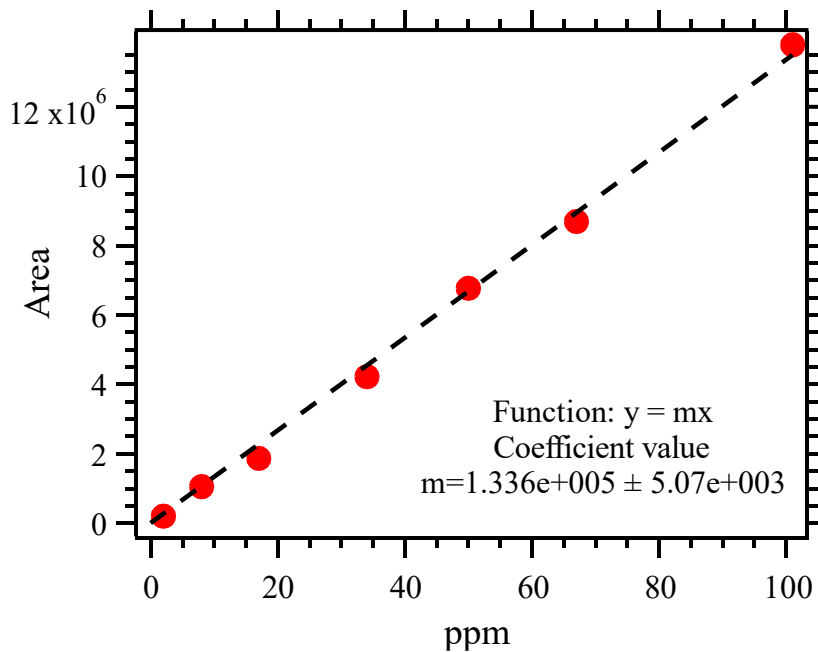
Figure 4.7: The calibration curve obtained for 1-pentene using a seven-point calibration

4.3.3   Alkane

This section presents a comparison of the experimental and simulated concentrations for various quench times. As noted earlier, we use the simulated case with the longest quench time to compare against the experimental values as a first approximation. The pressure trace for the longest simulated quench at 155.6 ms is shown in Figure 4.8 (a). The start of quench for the experimental samples is labeled in the zoomed-in view shown in Figure 4.8(b). Note that the experiments consist of six different runs whose quench was initiated at times shown in the figure. The computed values shown in the comparisons will be based on this one simulation.
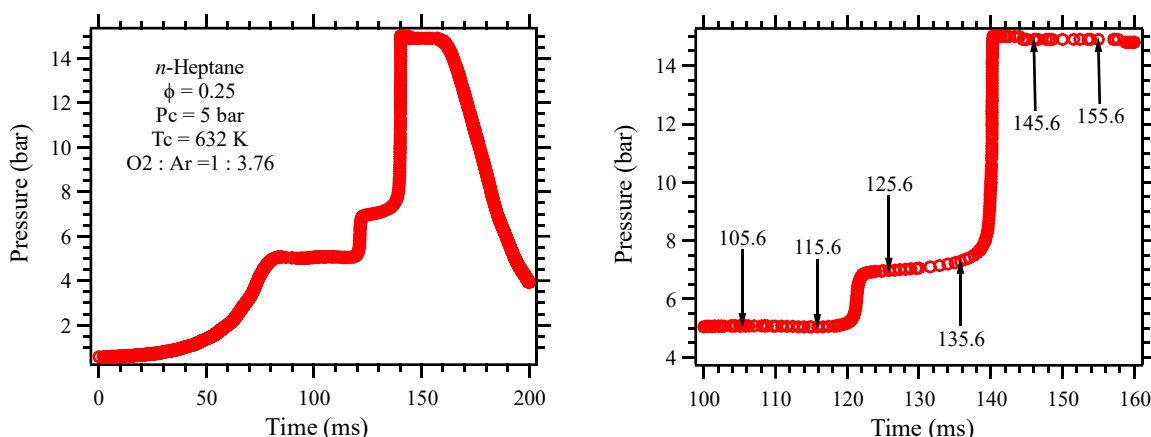
Figure 4.8: (a) Simulated pressure trace for a quenching time starting at 155.6 ms with (b) tags showing the six times where experimental quench was initiated.

This approach amounts to saying that the experimental and numerical quench is instantaneous.

The plot in Figure 4.9 shows the experimental and computed trends for the parent fuel consumption. Note that the experiment's first data point is for the quench starting at 105.6 ms, and the end of compression is 83.23 ms. At this time (105.6), the experiment has undergone the first-stage ignition. At the same time, the computations are still in the first-stage delay phase, i.e., the simulated mixture has been compressed but has not yet transitioned to the first-stage ignition. This nicely explains the difference between the experimental value (230 ppm) and the

computed *n*-heptane concentration (4751 ppm). The bulk of the fuel consumption takes place during the first-stage ignition. Once the simulation undergoes the first-stage ignition, the fuel concentration drops sharply. Specifically, at the instant of 122.5 ms, close to the end of the first-stage ignition, the simulated *n*-heptane concentration is equal to 300 ppm. Thus there is an excellent agreement (230 ppm experiment versus 300 ppm simulations) between the two cases right at the end of the first-stage ignition.
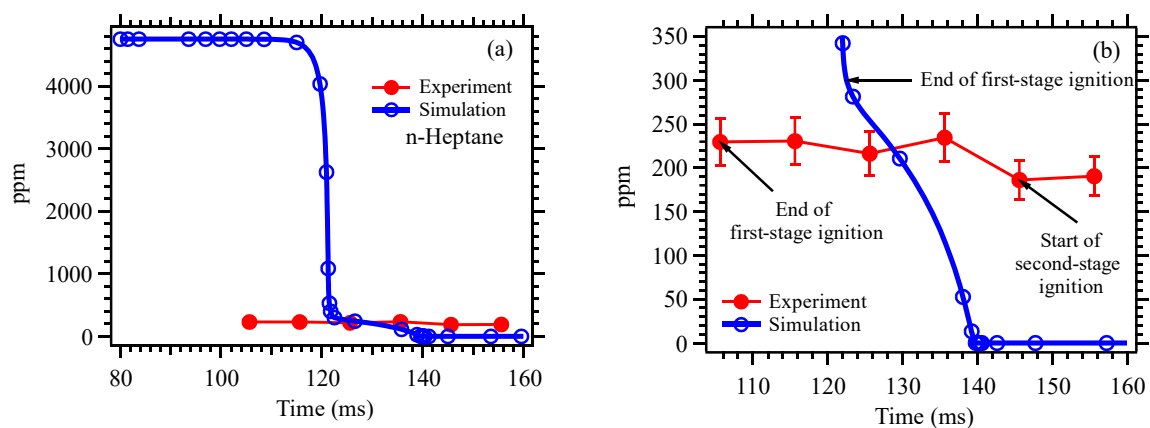
Figure 4.9: Experimental and simulated concentrations for n-heptane.

The experimental and computed trends for the *n*-heptane concentrations after the end of the first-stage ignition and the second-stage ignition delay $(122.5 < t < 131\ ms)$ show a difference in the fuel consumption trends. The experiments exhibit minimal fuel consumption during the second-stage delay period while the computed results point toward a continued fuel consumption. During the second-stage, this continued fuel consumption occurs at a significant but still smaller rate than what is observed during the first-stage ignition. The experimental trend for all the six data points also shows a minimal reduction with time during the second-stage delay. However, these variations are well within the limits of the experimental errors. The onset of the second-stage delay leads to complete fuel consumption in the computed results. The second-stage ignition onset is also evident in the experiments where the fuel concentration drops from 234 ppm at 135.6 ms to approximately 186 ms at 145.6 ms.

4.3.4 Olefins

Olefins with carbon numbers between three and six ($C_3 - C_6$) were detected in this work. They include propene, 2-butene, 1-pentene, and 1-hexene. Of these, only the last three, namely 2-butene, 1-pentene, and 1-hexene, were quantified in this work. The formation of lower alkenes seemed to be favored over higher carbon number counterparts. The peak observed experimental value for n-butene was found to be 85 ppm, while those for 1-pentene and 1-hexene were 32 ppm and 7.3 ppm, respectively.
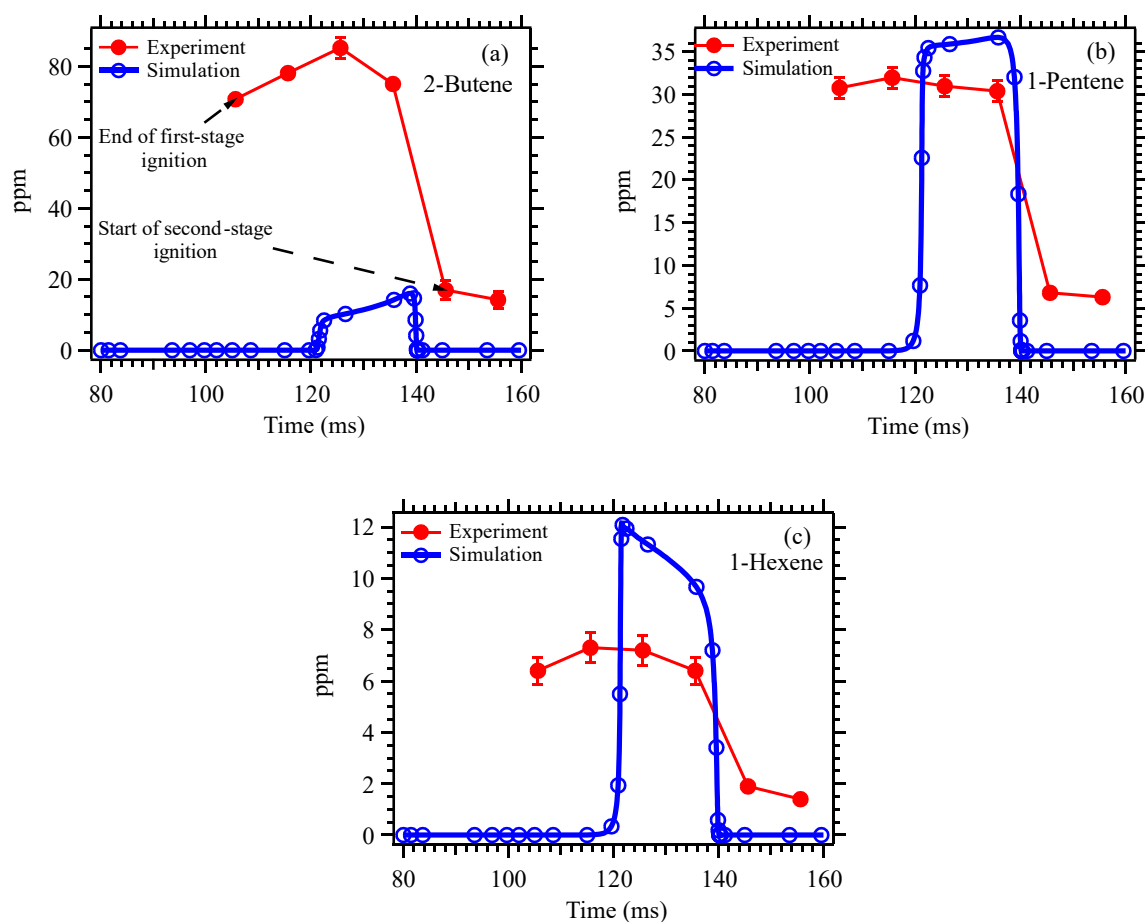
Figure 4.10: Experimental and simulated concentrations for olefins.

A very similar trend is observed for all three olefins. They initially show a slight increase during the second-stage induction period as time progresses and then begin to decrease right before

the onset of the second-stage ignition. All the three olefins drop to nearly a quarter of their values after the second-stage ignition sets in. The reduction continues through the progress of the second-stage ignition. The feature related to the buildup and consumption of olefinic species is captured very well by the simulations, including the magnitudes for the 1-pentene and 1-hexene concentrations. The 2-butene concentrations are, however, underpredicted, and the peak values differ by as much as a factor of four.

4.3.5 Aldehydes and Ketones

Saturated and unsaturated carbonyl compounds accounted for nearly half of the stable intermediates detected in this work. Aldehyde and ketone concentrations were among the highest and next only to the parent fuel concentration.
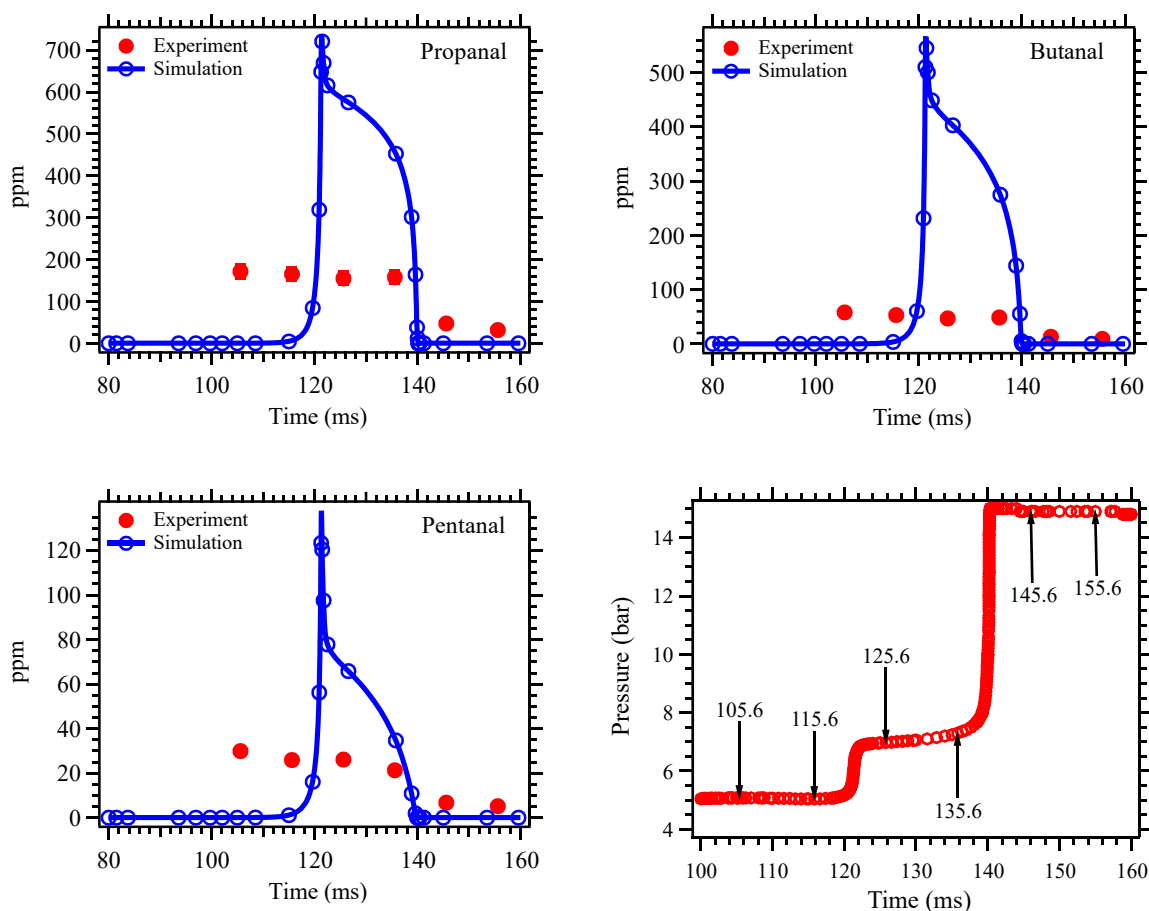
Figure 4.11: Experimental and simulated concentrations for aldehydes.

Saturated straight-chain aldehydes ranging from ethanal to pentanal were formed under the current test conditions. Hexanal was not present in measurable concentrations. Unsaturated aldehydes such as propenal and 2-butenal were also found. The quantification of aldehyde concentrations in this work was limited to the saturated ones and included propanal, butanal, and pentanal. Similar to the olefins, the lower carbon number aldehydes were formed in larger

quantities. Propanal was the most abundant, followed by butanal and pentanal during the second-stage induction period. The peak propanal concentration was 172 ppm for the experiments. Butanal and pentanal peak concentrations were 58 and 30 ppm, respectively.

The experimental aldehyde concentration, in general, remains nearly the same throughout the second-stage induction period with a very slight reduction with increasing time for all three components. The onset of the second-stage ignition leads to rapid consumption of 80% of the aldehyde component. The experiments have a remnant aldehyde concentration after the start of the second-stage because the quench takes place before the hot ignition is complete.

The simulations tend to overpredict the aldehyde concentrations during the second-stage induction period. They also exhibit a near-instantaneous increase to their peak values at approximately 120 ms, which corresponds to the onset of the first-stage ignition. The aldehyde consumption in the simulations continues throughout the second-stage induction delay and is almost complete before the beginning of the hot ignition. The difference in production and consumption rates during this time leads to a somewhat asymmetric peak shape in the simulations.
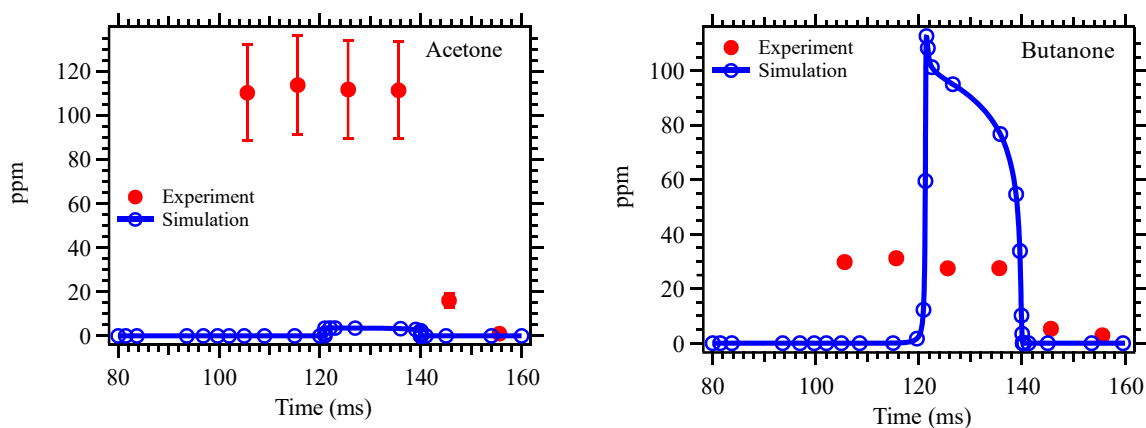
Figure 4.12: Experimental and simulated concentrations for ketones.

4.3.6 Cyclic Ethers

The formation of cyclic ethers during low-to-intermediate temperature hydrocarbon oxidation is a well-recognized feature in the combustion literature. The current test conditions are expected to produce intermediates with relatively large carbon numbers [24]. However, in this work, we detected and quantified the presence of somewhat smaller cyclic ethers such as propylene oxide and ethyloxirane. The experimental and computed results for the two compounds are shown in Figure 4.13. Other cyclic ethers could not be quantified due to their low signal-to-noise ratios and limited availability of pure compounds to be used for calibration. The production of cyclic ethers is attributed to the chain propagation reactions involving the hydroperoxyalkyl radical (QOOH). Curran et al. [24] state that while at low temperatures, the chain branching proceeds through pathways involving the ketohydroperoxide species increasing temperature leads to an increase in the chain propagation reactions involving the hydroperoxyalkyl radical [24]. Therefore, cyclic ether production may be related to a shift in the chemistry from the low to the intermediate/high-temperature regime. The computed results support this statement. The propylene oxide and ethyloxirane concentrations peak at much longer times (~136 ms, T~920 K) than the carbonyl compounds and olefins (~120 ms, T~650 K) when the system temperature is much higher. The experimental results for propylene oxide do indeed also confirm this trend. Its concentration continues to rise to a time of 135.6 ms. The increasing trend continues through the entire second-stage delay and right up to the onset of the hot second-stage ignition, unlike the other classes of compounds that begin to reduce in concentration by this time (i.e., during the second stage-delay). However, the trend for ethyloxirane is similar to the other classes and exhibits a peak at around 115.6 ms.

The experimental and computed results for propylene oxide are in fair agreement after the onset of the first-stage ignition and show an increasing trend throughout the first-stage delay. Note that the peak values are also well predicted (within a factor of two) by the simulations. The computed results for ethyloxirane are, however, lower compared to the experiments. Note, however, that the absolute differences are not too significant (less than 8ppm). The most impressive aspect is the mechanism's ability to predict the one order of magnitude difference between the propylene oxide and ethyloxirane concentrations as observed in the experimental data.
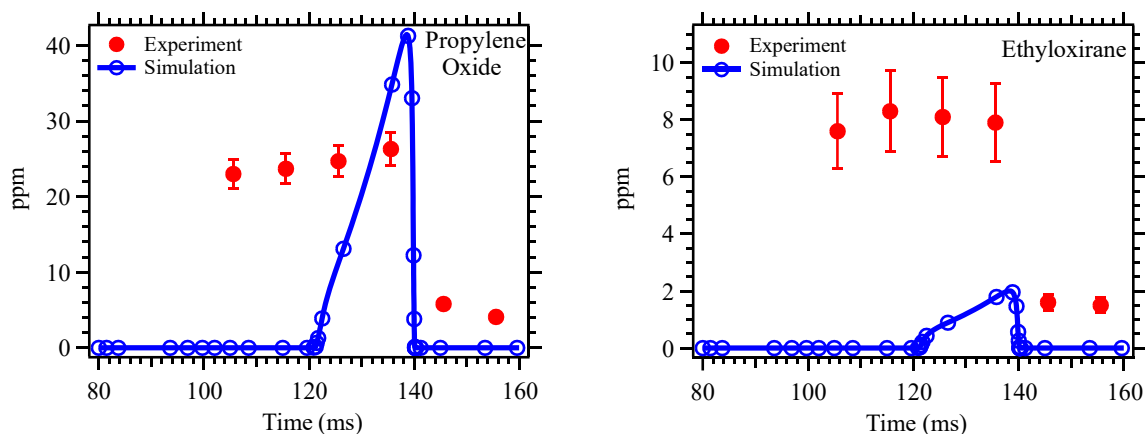
Figure 4.13: Experimental and simulated concentrations for cyclic ethers.

4.4   Quench End Point Analysis

4.4.1   Quench End Point Definition

The previous set of comparisons for experimental and simulated intermediate species concentrations used the single most extended simulation (start of quench = 155.6 ms) and plotted the computed species profile as a function of time. The experimental data were plotted on the same graph against their respective start of quench time. This enabled a simple explanation of trends in terms of the various ignition phenomena observed computationally (e.g., the onset of first or second-stage delay). The more rigorous approach is to compare the end point concentrations for both the experimental and simulated cases. The end point for the simulations for all cases is set as 500 ms and effectively corresponds to a complete quench both experimentally and computationally. Note that in real life, the sample is collected a few minutes after the full quench. An example of the end point definition is shown in Figure 4.14.
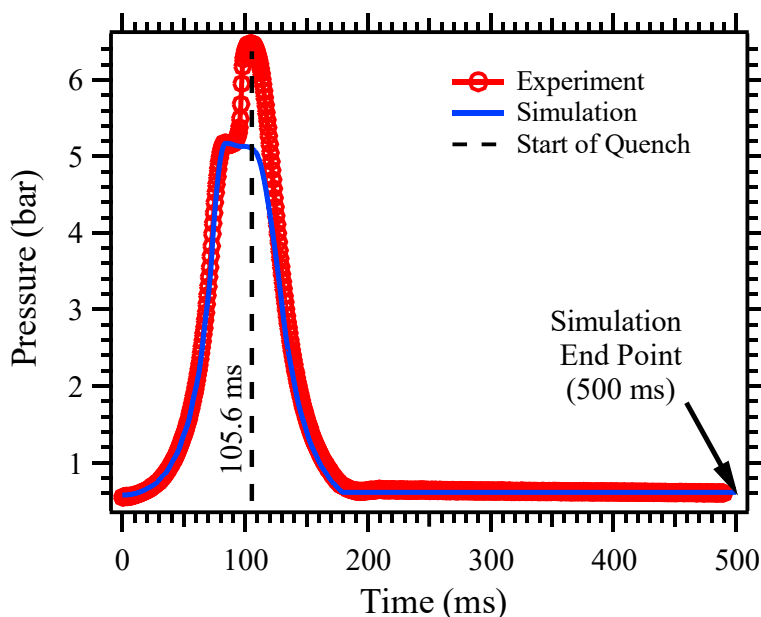
Figure 4.14: Illustration of simulated end point used for obtaining species concentration.

The comparison presented in the figure again highlights the unique operating capabilities of this machine and shows the importance of recording reactor volume profiles. It would have been impossible to simulate the quenching process without access to reactor volume data. Using experimental pressure traces to estimate volume profile, as is often done in the current literature, would lead to erroneous results once heat release begins contributing to the pressure changes.

4.4.2 Quench PressureTraces

The complete set of six experimental quench pressure traces for tests starting at identical initial conditions are shown in Figure 4.15.
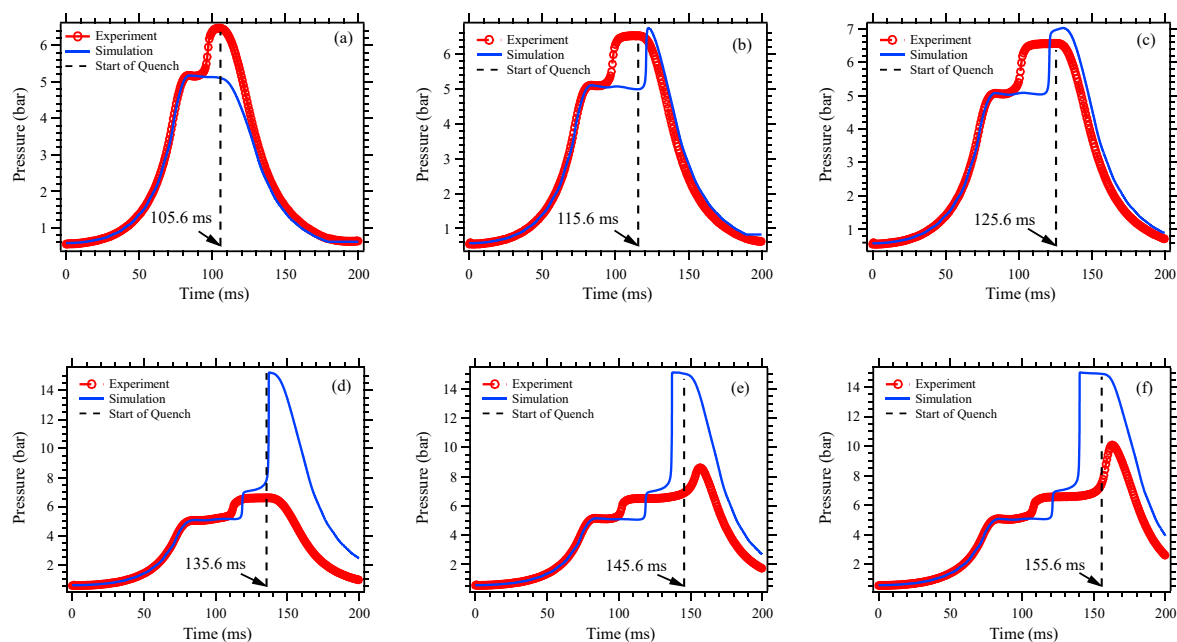
Figure 4.15: The set of six quench experiments along with the corresponding simulated results.

The subplots (a)–(c) in the top row for Figure 4.15 represent conditions where the first-stage ignition has occurred in all three experiments. Still, only two sets of computed values, (b) and (c), exhibit the first-stage ignition. This implies that the mechanism has a somewhat reduced reactivity preceding the first-stage ignition. Note that there is an excellent agreement for the

magnitude of the first-stage pressure rise between the experimental and computed pressure traces across all experiments. Subplots (d)–(e) show conditions approaching the end of the second-stage delay and the onset of hot ignition for the experiments. For these conditions, the simulations seem to have entered the hot ignition phase much before the experiments. Therefore the second-stage reactivity is much higher for the kinetic model.

4.4.3 Species Concentrations at Quench End Point

In addition to the global pressure markers, this work also acquired the end point species concentrations. Six end point concentrations corresponding to each of the quench times are shown in Figure 4.16. Filled symbols and continuous lines in Figure 4.16 represent the experimental values, while empty symbols and dashed lines represent the computed values.

The comparative trend in Figure 4.16 shows that the peak values for the two olefinic species, pentene, and hexene, are predicted reasonably well by the simulations. However, the 2-butene concentrations are significantly underpredicted. The model predictions for peak aldehyde concentrations are, in general, higher by a factor of 2.0–3.0. The trend for the variation of aldehyde concentrations is reasonably well predicted and can be explained by the system's state during the start of the quench. In terms of the various induction and ignition stages, the system's state is provided in a tabular format inserted within Figure 4.16. This makes it easier to follow the observed trends for each of the species. Note that the last three quench points for the simulated results across all the species show negligible variation because they represent conditions after the hot second-stage ignition. The most significant disagreement between the model and experimental results is that for acetone. The model significantly underpredicts the acetone concentrations.

Time	Experiment	Simulation
105.6	2nd stage induction	1st stage induction
115.6	2nd stage induction	2nd stage induction
125.6	2nd stage induction	2nd stage induction
135.6	2nd stage induction	Post 2nd stage ignition
145.6	Onset 2nd stage ignition	Post 2nd stage ignition
155.6	Post 2nd stage ignition	Post 2nd stage ignition
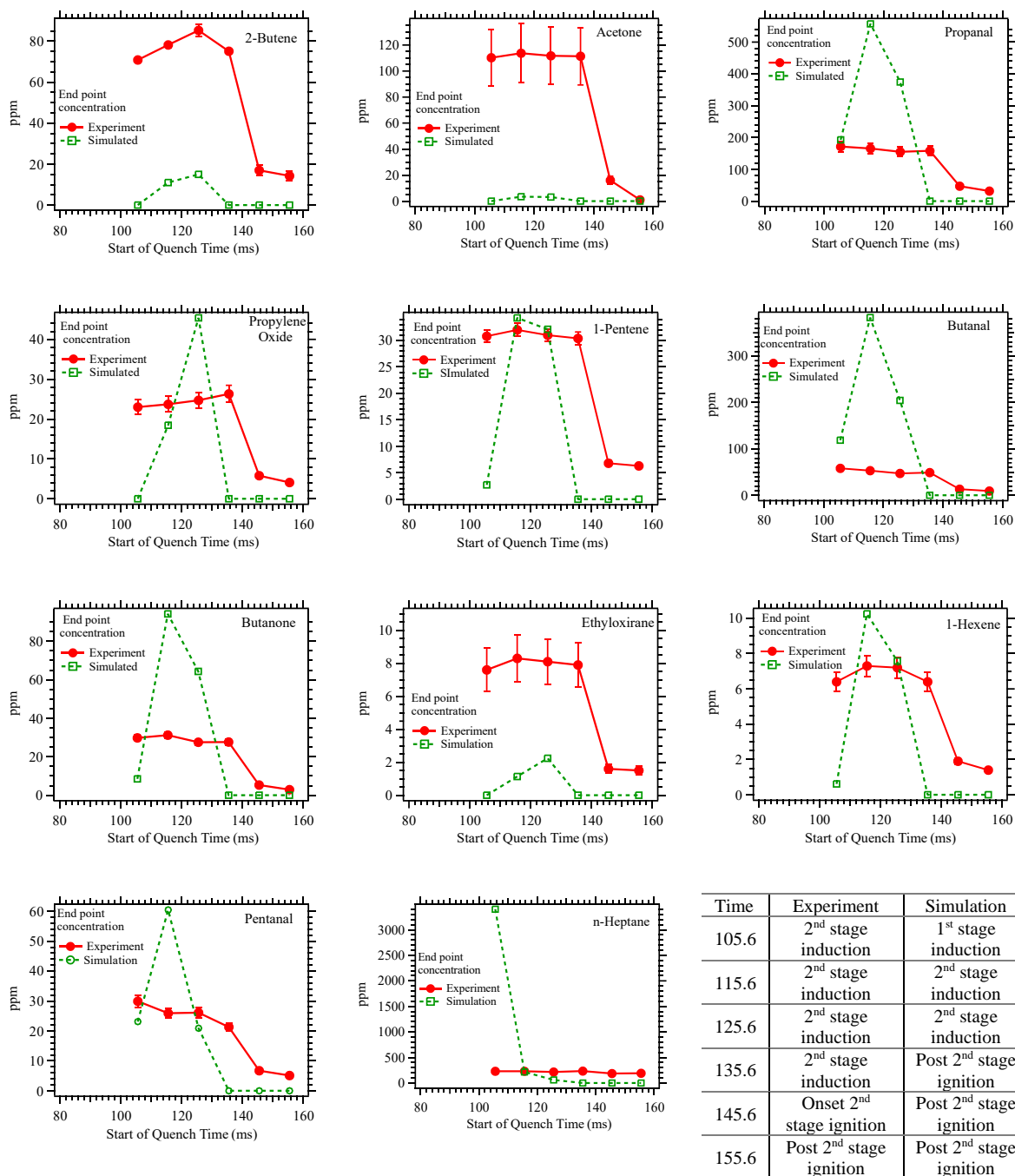
Figure 4.16: Experimental and simulated end point species concentrations.

4.5   Conclusion

A rapid compression expansion machine (RCEM) was developed to study species evolution during the homogeneous gas-phase autoignition process. The speciation analysis in this research detected multiple stable intermediate species across a wide range of chemical classes such as alkenes, aldehydes, ketones, and ethers. This work also provides quantitative measurements for eleven intermediate species and compares them to results from an existing detailed chemical kinetic mechanism in the literature. Species of the same chemical group show similar trends for variation with the start of quench times, although there were differences in their relative concentrations.

Comparing the experimental speciation results to numerical predictions was possible due to the ability to obtain reactor volume profiles throughout the compression and quench process, unique to this device. The experimental end point species concentrations were in fair agreement with numerical model predictions for most species except 2-butene and acetone. The bulk of the fuel consumption occurred during the first-stage ignition for both the experiments and simulations. The peak concentrations for cyclic ethers in the experiments occurred later during the second-stage induction period at higher temperatures, possibly indicating a transitory region between low and intermediate temperature chemistry.

.

5   Summary and Future Study Recommendations

This novel RCEM marks a new generation of RCM's used as homogeneous reactors to study combustion chemical kinetics. The results provided insights into autoignition characteristics through a wide range of combustion conditions. The ability to obtain experimental ignition delay data for fuel-lean mixtures at low-to-intermediate compressed temperatures was demonstrated. Such data is vital for developing future energy conversion technologies that rely on the autoignition of reactive fuel mixtures. As such, this RCEM is an excellent tool to study the autoignition of conventional and alternative fuels.

The RCEM incorporated key design features that allow repeatability of experimental runs and a wide range of test conditions. Important design features include a magnetically driven piston rod, enabling fast compression and expansion of the reactor, infinitely variable compression ratio, and minimal system vibrations and background noise. The programmable compression ratios eliminate the tedious repeated manual adjustments of shims and spacers and increase operational efficiency. This machine also has negligible vibrations at EOC, leading to improved data quality.

Autoignition and speciation experimentation for n-heptane were conducted using the RCEM. Data obtained from these experiments revealed a two-stage ignition and the negative temperature coefficient (NTC) phenomenon for the ignition delay times. The NTC region was very well captured for the current combustion conditions indicating the utility of the current RCEM. Experimental runs for n-heptane were conducted with equivalence ratios of 0.20, 0.25, 0.35, and 0.50. Compressed pressures were between 3–5.5 bar, and compressed temperatures were between 593–745 K. The oxidizer use in these experiments comprised a mixture of oxygen and argon in a molar proportion of 1:3.76. The trends for the variation of ignition delay times

with respect to equivalence ratio, compressed pressure, and temperature were consistent with expected results for *n*-heptane. Numerical simulations were conducted using detailed chemistry and volume profiles that include pre and post heat loss effects. The LLNL mechanism for *n*-heptane [24-26] agrees well with experimental ignition delay times at higher compressed temperatures. Still, discrepancies are apparent at lower compressed temperatures. The simulation models were able to predict the temperature span indicative of the NTC region accurately.

Qualitative and quantitative GC-MS analysis of quenched products during various stages of ignition was conducted through rapid expansion following the end of compression. Concentration profiles of different stable intermediate species identified show mixed agreement between experimental and simulated results and can guide potential improvement for the detailed chemical mechanism. All simulated species profiles except the parent fuel show peak concentrations after the onset of the first-stage ignition and are rapidly consumed once the second-stage ignition starts.

This study's new RCEM has shown that it can retrieve experimental data across a wide range of combustion conditions for the primary reference fuel component *n*-heptane via ignition delay and speciation data. As a result, future use of the machine can include experimental gasoline-like and diesel-type fuels. In addition, studying gaseous fuel components is also a possibility.

Computational fluid dynamic (CFD) simulations should be conducted to examine the reactor's velocity, temperature, and species concentration fields. A CFD study can aid the development of improved heat loss models.

The RCEM can also be made capable of flame propagation studies by fitting the detachable reactor head with an infrared transparent window to provide optical access. In addition, using

an IR camera will allow for better qualitative and quantitative characterization of the RCEM temperature field.

6 References Cited

[1] R.J. Kee, M.E. Coltrin, P. Glarborg, in: Chemically reacting flow: Theory and practice, John Wiley & Sons, 2003, p 653.

[2] S.R. Turns, in: An introduction to combustion: Concepts and applications, 3 ed.; McGraw-Hill, New York, 2012, p 206.

[3] P. Dagaut, M. Reuillon, M. Cathonnet, Experimental-study of the oxidation of n-heptane in a jet-stirred reactor from low-temperature to high-temperature and pressures up to 40-atm, Combustion and Flame 101 (1-2) (1995) 132-140.

[4] J.P. Longwell, M.A. Weiss, High temperature reaction rates in hydrocarbon combustion, Industrial & Engineering Chemistry 47 (1955) 1634-1643.

[5] S.R. Turns, in: An introduction to combustion: Concepts and applications, 3 ed.; McGraw-Hill, New York, 2012, p 197.

[6] C. Lee, S. Vranckx, K.A. Heufer, S.V. Khomik, Y. Uygun, H. Olivier, R.X. Fernandes, On the chemical kinetics of ethanol oxidation: Shock tube, rapid compression machine and detailed modeling study, Zeitschrift Fur Physikalische Chemie-International Journal of Research in Physical Chemistry & Chemical Physics 226 (1) (2012) 1-27.

[7] D. Healy, M.M. Kopp, N.L. Polley, E.L. Petersen, G. Bourque, H.J. Curran, Methane/n-butane ignition delay measurements at high pressure and detailed chemical kinetic simulations, Energy & Fuels 24 (2010) 1617-1627.

[8] D.J. Hucknall, in: Chemistry of hydrocarbon combustion, Chapman and Hall, London, 1985, p 101.

[9] C.J. Sung, H.J. Curran, Using rapid compression machines for chemical kinetics studies, Progress in Energy and Combustion Science 44 (2014) 1-18.

[10] J. Wurmel, E.J. Silke, H.J. Curran, M.S.O. Conaire, J.M. Simmie, The effect of diluent gases on ignition delay times in the shock tube and in the rapid compression machine, Combustion and Flame 151 (1-2) (2007) 289-302.

[11] H. Hu, J. Keck, Autoignition of adiabatically compressed combustible gas mixtures, SAE International, 1987.

[12] D. Healy, D.M. Kalitan, C.J. Aul, E.L. Petersen, G. Bourque, H.J. Curran, Oxidation of c1-c5 alkane quinternary natural gas mixtures at high pressures, Energy & Fuels 24 (2010) 1521-1528.

[13] X. Hui, K. Kumar, C.J. Sung, T. Edwards, D. Gardner, Experimental studies on the combustion characteristics of alternative jet fuels, Fuel 98 (2012) 176-182.

[14] K.G. Falk, The ignition temperatures of hydrogen-oxygen mixtures, Journal of the American Chemical Society 28 (11) (1906) 1517-1534.

[15] L.H.S. Roblee, A technique for sampling reaction intermediates in a rapid compression machine, Combustion and Flame 5 (3) (1961) 229-234.

[16] S. Drost, R. Schiessl, M. Werler, J. Sommerer, U. Maas, Ignition delay times of polyoxymethylene dimethyl ether fuels (ome2 and ome3) and air: Measurements in a rapid compression machine, Fuel 258 (2019) 6.

[17] S. Heyne, A. Roubaud, M. Ribaucour, G. Vanhove, R. Minetti, D. Favrat, Development of a natural gas reaction mechanism for engine simulations based on rapid compression machine experiments using a multi-objective optimisation strategy, Fuel 87 (13-14) (2008) 3046-3054.

[18] J. Pan, Hu, Zhen, Wei, Haiqiao, Pan, Mingzhang, Liang, Xingyu, Shu, Gequn, & Zhou, Lei. , Understanding strong knocking mechanism through high-strength optical rapid compression machines, Combustion and Flame 202 (2019) 1–15.

[19] G. Kukkadapu, K. Kumar, C.J. Sung, M. Mehl, W.J. Pitz, Experimental and surrogate modeling study of gasoline ignition in a rapid compression machine, Combustion and Flame 159 (10) (2012) 3066-3078.

[20] G. Kukkadapu, K. Kumar, C.J. Sung, M. Mehl, W.J. Pitz, Autoignition of gasoline and its surrogates in a rapid compression machine, Proceedings of the Combustion Institute 34 (2013) 345-352.

[21] J. Chung, S. Lee, H. An, S. Song, K.M. Chun, Rapid-compression machine studies on two-stage ignition characteristics of hydrocarbon autoignition and an investigation of new gasoline surrogates, Energy 93 (2015) 1505-1514.

[22] G. Mittal, C.J. Sung, Aerodynamics inside a rapid compression machine, Combustion and Flame 145 (1-2) (2006) 160-180.

[23] G. Mittal, C.J. Sung, A rapid compression machine for chemical kinetics studies at elevated pressures and temperatures, Combustion Science and Technology 179 (3) (2007) 497-530.

[24] H.J. Curran, P. Gaffuri, W.J. Pitz, C.K. Westbrook, A comprehensive modeling study of n-heptane oxidation, Combustion and Flame 114 (1) (1998) 149-177.

[25] M. Mehl, W.J. Pitz, M. Sjöberg, J.E. Dec, Detailed kinetic modeling of low-temperature heat release for prf fuels in an HCCI engine, SAE International, 2009-01-1806, 2009.

[26] M. Mehl, W.J. Pitz, C.K. Westbrook, H.J. Curran, Kinetic modeling of gasoline surrogate components and mixtures under engine conditions, Proceedings of the Combustion Institute 33 (1) (2011) 193-200.

[27] S.S. Goldsborough, S. Hochgreb, G. Vanhove, M.S. Wooldridge, H.J. Curran, C.-J. Sung, Advances in rapid compression machine studies of low- and intermediate-temperature autoignition phenomena, Progress in Energy and Combustion Science 63 (2017) 1-78.

[28] P. Park, Rapid compression machine measurements of ignition delays for primary reference fuels. Massachusetts Institute of Technology, 1990.

[29] CANopen, Canopen - the standardized embedded network. https://www.can-cia.org/can-knowledge/canopen/canopen/ (12-Oct-2016)

[30] Ansys®, Fluent

[31] Labview®, National instruments

[32] A.J. Smallbone, W. Liu, C.K. Law, X.Q. You, H. Wang, Experimental and modeling study of laminar flame speed and non-premixed counterflow ignition of n-heptane, Proceedings of the Combustion Institute 32 (2009) 1245-1252.

[33] C.D. Yao, C.H. Cheng, S.Y. Liu, Z.Y. Tian, J. Wang, Identification of intermediates in an n-heptane/oxygen/argon low-pressure premixed laminar flame using synchrotron radiation, Fuel 88 (9) (2009) 1752-1757.

[34] D.J. Vermeer, J.W. Meyer, A.K. Oppenheim, Auto-ignition of hydrocarbons behind reflected shock-waves, Combustion and Flame 18 (3) (1972) 327-336.

[35] J.F. Griffiths, K.J. Hughes, M. Schreiber, C. Poppe, A unified approach to the reduced kinetic modeling of alkane combustion, Combustion and Flame 99 (3-4) (1994) 533-540.

[36] A. Cavaliere, A. Ciajolo, A. Danna, R. Mercogliano, R. Ragucci, Autoignition of n-heptane and n-tetradecane in engine-like conditions, Combustion and Flame 93 (3) (1993) 279-286.

[37] H.Y. Guang, Z. Yang, Z. Huang, X.C. Lu, Experimental study of n-heptane ignition delay with carbon dioxide addition in a rapid compression machine under low-temperature conditions, Chin. Sci. Bull. 57 (30) (2012) 3953-3960.

[38] T. Javed, C. Lee, M. AlAbbad, K. Djebbi, M. Beshir, J. Badra, H. Curran, A. Farooq, Ignition studies of n-heptane/iso-octane/toluene blends, Combustion and Flame 171 (2016) 223-233.

[39] E.J. Silke, H.J. Curran, J.M. Simmie, The influence of fuel structure on combustion as demonstrated by the isomers of heptane: A rapid compression machine study, Proceedings of the Combustion Institute 30 (2005) 2639-2647.

[40] D.M.A. Karwat, S.W. Wagnon, M.S. Wooldridge, C.K. Westbrook, Low-temperature speciation and chemical kinetic studies of n-heptane, Combustion and Flame 160 (12) (2013) 2693-2706.

[41] R. Minetti, M. Carlier, M. Ribaucour, E. Therssen, L.R. Sochet, A rapid compression machine investigation of oxidation and auto-ignition of n-heptane - measurements and modeling, Combustion and Flame 102 (3) (1995) 298-309.

[42] S. Tanaka, F. Ayala, J.C. Keck, J.B. Heywood, Two-stage ignition in HCCI combustion and HCCI control by fuels and additives, Combustion and Flame 132 (1-2) (2003) 219-239.

[43] C.K. Westbrook, W.J. Pitz, J.E. Boercker, H.J. Curran, J.F. Griffiths, C. Mohamed, M. Ribaucour, Detailed chemical kinetic reaction mechanisms for autoignition of isomers of heptane under rapid compression, Proceedings of the Combustion Institute 29 (2002) 1311-1318.

[44] H. An, J. Chung, S. Lee, S. Song, The effects of hydrogen addition on the auto-ignition delay of homogeneous primary reference fuel/air mixtures in a rapid compression machine, International Journal of Hydrogen Energy 40 (40) (2015) 13994-14005.

[45] J. Andrae, D. Johansson, P. Bjornbom, P. Risberg, G. Kalghatgi, Co-oxidation in the auto-ignition of primary reference fuels and n-heptane/toluene blends, Combustion and Flame 140 (4) (2005) 267-286.

[46] R. Di Sante, Measurements of the auto-ignition of n-heptane/toluene mixtures using a rapid compression machine, Combustion and Flame 159 (1) (2012) 55-63.

[47] D.M.A. Karwat, S.W. Wagnon, M.S. Wooldridge, C.K. Westbrook, On the combustion chemistry of n-heptane and n-butanol blends, The Journal of Physical Chemistry A 116 (51) (2012) 12406-12421.

[48] Ansys®, Chemkin-pro

[49] A.E. Lutz, R.J. Kee, J.A. Miller, in: Sandia National Laboratories: Livermore, 1997; Vol. SAND87-8248.

[50] J.F. Griffiths, C. Mohamed, in: Low-temperature combustion and autoignition, M. J. Pilling, (Ed.) Elsevier, Amsterdam, 1997, Vol. 35, p 574.

[51] J.F. Griffiths, C. Mohamed, in: Low-temperature combustion and autoignition, M. J. Pilling, (Ed.) Elsevier, Amsterdam, 1997, Vol. 35, p 653.

[52] S.E. Stein, W. Wallace, NIST/EPA/NIH mass spectral library (NIST 17) and NIST mass spectral search program (version 2.3)

[53] P.G. Ashmore, in: Catalysis and inhibition of chemical reactions, Butterworths, London, 1963, pp 329-360.

[54] C. Morley, M.J. Pilling, in: Comprehensive chemical kinetics: Low-temperature combustion and autoignition, Elsevier, 1997, Vol. 35, pp IX-XX.

[55] G.-M. Côme, Gas-phase thermal reactions, Kluwer Academic Publishers, 2001

[56] P.G. Ashmore, in: Catalysis and inhibition of chemical reactions, Butterworths, London, 1963, pp 257-265.

7 Appendices

7.1 Compressed Temperature Estimation

The estimation of compressed temperature takes into account the variation of specific heat with temperature for the fuel oxidizer mixture. The specific heat data utilized in the calculations is in the form of a polynomial function of temperature. In particular, the molar heat capacities c_p/R is expressed as a five-term polynomial of fourth order in temperature given as[1]:

$$c_p/R = a_1 + a_2T + a_3T^2 + a_4T^3 + a_5T^4 \qquad 7.1$$

The constants a_i are specified as two sets of seven polynomial coefficients. Two different polynomials are used: one for the low-temperature range (a_1–a_7) and the other (a_8–a_{14}) for the high-temperature range. Only the first five coefficients for each temperature range are used to calculate the specific heat.

Table 7.1: Polynomial coefficients used in calculations of compressed temperature LLNL mechanism (Curran et al., 1998, Mehl et al., 2009, Mehl et al., 2011)

a_1	a_2	a_3	a_4	a_5
n-Heptane				
2.22148969E+01	3.47675750E-02	-1.18407129E-05	1.83298478E-09	-1.06130266E-13
a_6	a_7	a_8	a_9	a_{10}
-3.42760081E+04	-9.23040196E+01	-1.26836187E+00	8.54355820E-02	-5.25346786E-05
a_{11}	a_{12}	a_{13}	a_{14}	
1.62945721E-08	-2.02394925E-12	-2.56586565E+04	3.53732912E+01	
Oxygen				
a_1	a_2	a_3	a_4	a_5
0.03697578E+02	0.06135197E-02	-0.01258842E-05	0.01775281E-09	-0.01136435E-13
a_6	a_7	a_8	a_9	a_{10}
-0.01233930E+05	0.03189166E+02	0.03212936E+02	0.01127486E-01	-0.05756150E-05
a_{11}	a_{12}	a_{13}	a_{14}	
0.01313877E-07	-0.08768554E-11	-0.01005249E+05	0.06034738E+02	
Argon				
a_1	a_2	a_3	a_4	a_5
0.02500000E+02	0.00000000E+00	0.00000000E+00	0.00000000E+00	0.00000000E+00
a_6	a_7	a_8	a_9	a_{10}
-0.07453750E+04	0.04366000E+02	0.02500000E+02	0.00000000E+00	0.00000000E+00
a_{11}	a_{12}	a_{13}	a_{14}	
0.00000000E+00	0.00000000E+00	-0.07453750E+04	0.04366000E+02	

---

[1] The CHEMKIN thermodynamic database. R.J. Kee, F.M. Rupley, and J.A. Miller. Sandia Report SAND87-8215B

The procedure for calculating the compressed temperature is shown in Figure 7.1. Note that these calculations are carried out in a Matlab®[2] script and assume that no reactions occur prior to the end of compression.

```
┌─────────────────────────────────────────────┐
│ Input Data to Matlab Calculations:           │
│   Initial Conditions: (P_0, T_0, X_{i,0})    │
│   Experiment Datafile:(time, pressure,        │
│     Encoder Pulses)                           │
│   Parameters: Stroke, V_add, Heatloss         │
└─────────────────────────────────────────────┘
```

Calculated: End of compression time
Calculated: Volume as a function of time
Known: Sampling interval Δt

Loops start
t=0
Increment Δt

Known: $V(t+\Delta t)$
Calculate: $\gamma(t)$, $P(t+\Delta t)$, $T(t+\Delta t)$

Loop ends
when time equals
End of Compression (EOC)

Is Calculated P=
Experimental P at EOC

No → Adjust V_{add}

Yes
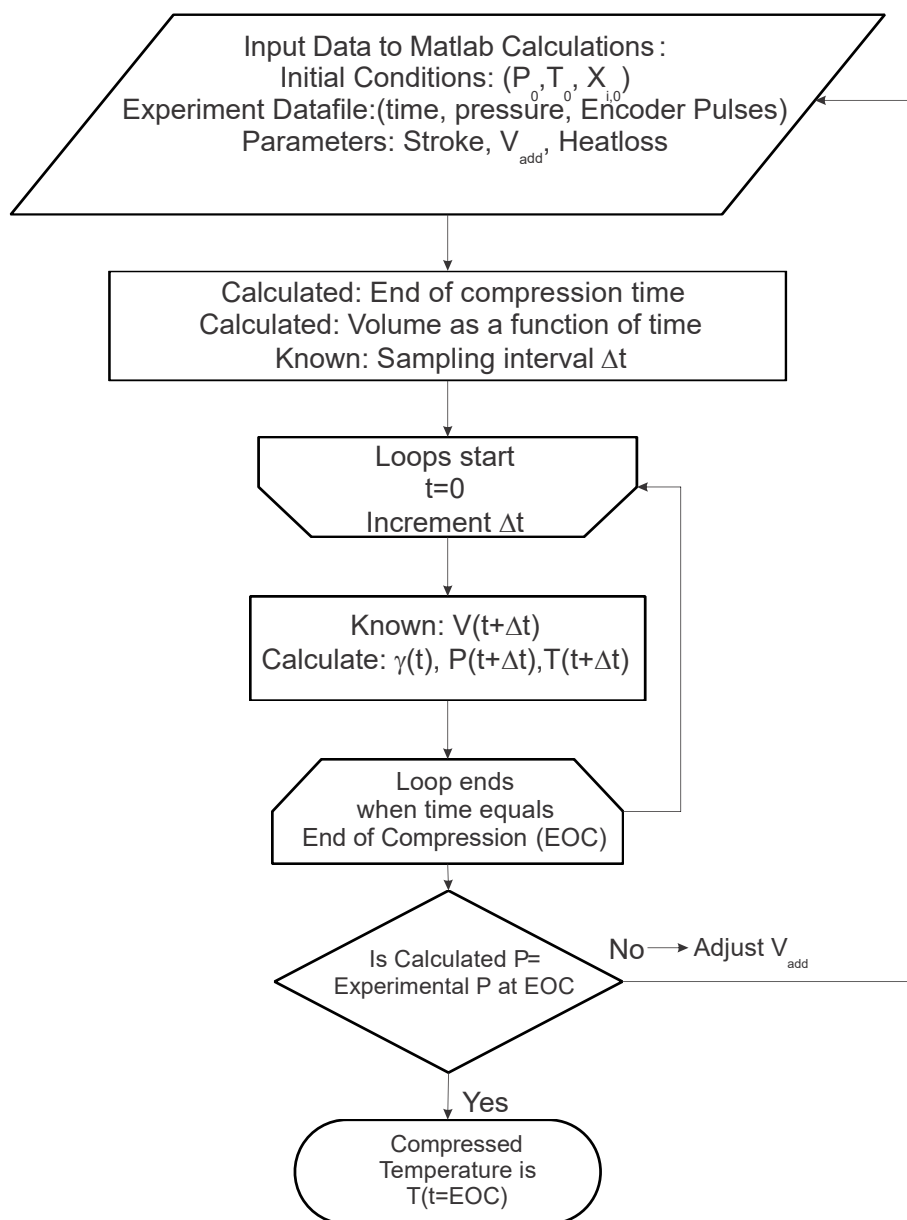
Compressed
Temperature is
T(t=EOC)

Figure 7.1: Illustration of procedure used to calculate compressed temperatures

[2] The MathWorks, Inc. MATLAB R2020b

7.2   Uncertainty Analysis for GC-MS Speciation Results

The quantitative speciation results for the identified components were based on the external standard method. A multipoint calibration curve relating the known concentrations to their respective peak areas was constructed for each of the species. The individual calibration curves used in this work are shown in Figure 7.2 (Butene, Acetone, Propanal, Propylene Oxide, Pentene, and Butanal) and Figure 7.3 (2-Butanone, Ethyloxirane, Hexene, and Pentanal). Two separate figures are used for clarity of presentation. The calibration plots show the experimental data points along with a straight line-fit that passes through the origin. A 95% confidence interval estimate of the slope of the fitted line is provided with each plot. The fit is accompanied by two dotted lines indicating the prediction bands. The prediction interval is defined as: "The interval estimate for the value of the target variable for an individual member of the population using the fitted regression model[3]." Note that only one run for each concentration value was carried out for this work due to the extended test and preparation times. It can be safely assumed that the scatter around a given concentration value would follow a normal distribution.

Note that in this work, there exist uncertainties in both the x (concentration) and the y (area under the curve) variables. The absolute pressure gauge used to manometrically prepare the gaseous mixture has a full-scale accuracy of $\pm$ 0.5 % and a resolution of 0.01 inches of mercury. The estimated error in measuring the liquid component injected into this gaseous mixture is no more than 5%. Note that microliter syringes were used to first inject the liquid component into a vacuumed container of known volume to enable flash-evaporation. As such, the uncertainty in the stated ppm is estimated to be of the order of 5%.

---

[3] Handbook of Regression Analysis. Samprit Chatterjee and Jeffrey S. Simonoff. Wiley Handbooks in Applied Statistics. Vol 5 (2012)
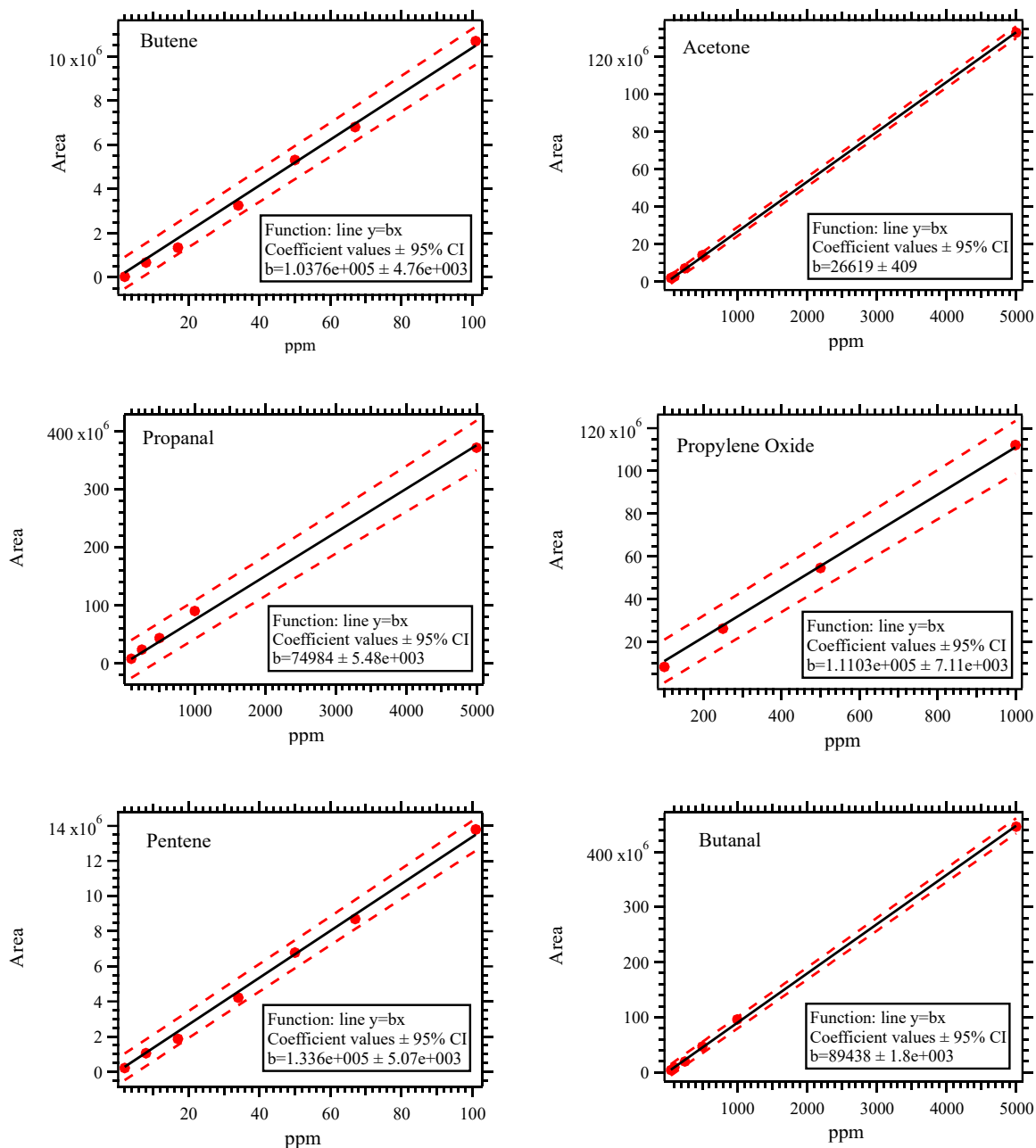
Figure 7.2: Calibration curves for Butene, Acetone, Propanal, Propylene Oxide, Pentene, and Butanal
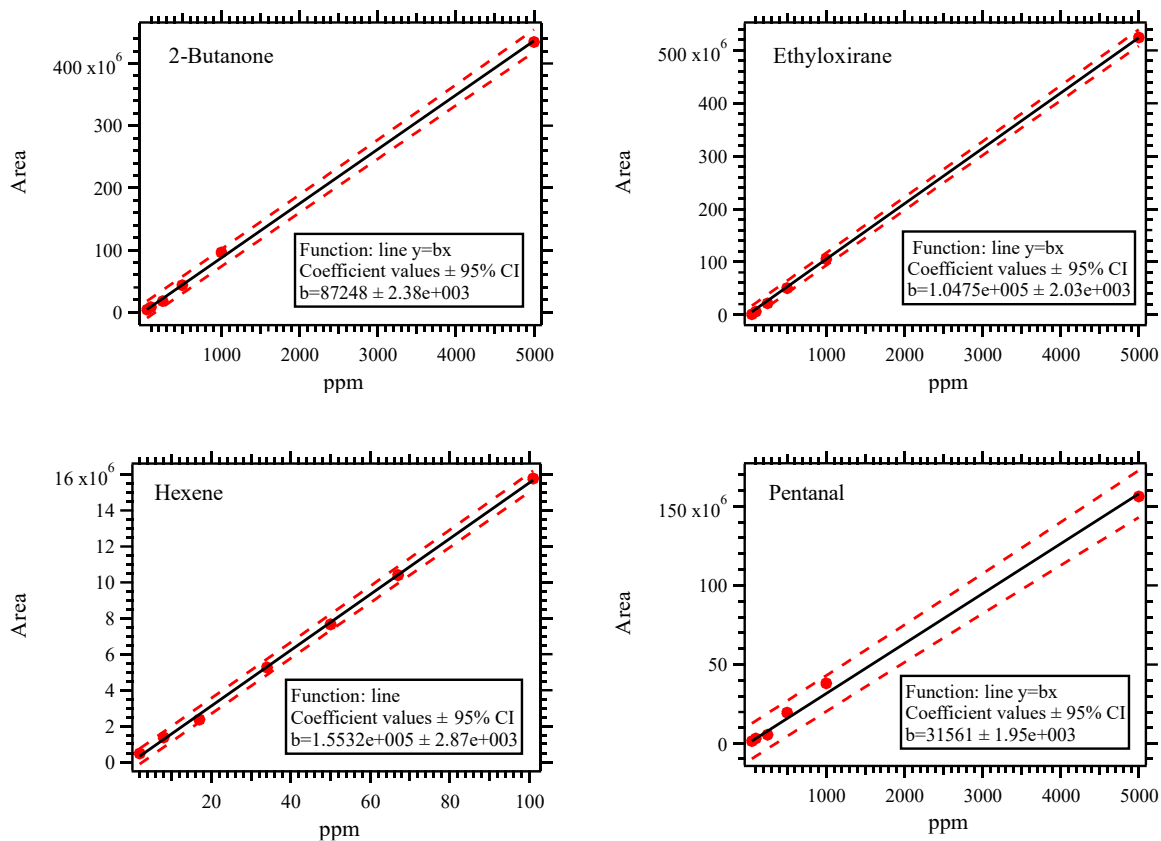
Figure 7.3: Calibration curves for 2-Butanone, Ethyloxirane, Hexene, and Pentanal

Table 7.2:Experimentally specified and calculated concentrations for linear calibration curves shown in Figure 7.2 and Figure 7.3

Specified	Calculated	% Diff	Specified	Calculated	% Diff
Butene			Butanal		
2	0.33	-84%	50	44	-13%
8	6.49	-19%	100	97	-3%
17	12.96	-24%	250	207	-17%
34	31.39	-8%	500	495	-1%
50	51.17	2%	1000	1014	1%
67	65.61	-2%	5000	4716	-6%
101	103.05	2%			
			2-Butanone		
Acetone			0	0	% Diff
50	76	52%	50	45	-9%
100	109	9%	100	89	-11%
250	271	8%	250	193	-23%
500	534	7%	500	468	-6%
5000	4995	0%	1000	1032	3%
			5000	4661	-7%
Propanal					
100	109	9%	Ethyloxirane		
250	318	27%	50	6	-87%
500	583	17%	100	57	-43%
1000	1203	20%	250	208	-17%
5000	4948	-1%	500	490	-2%
			1000	1022	2%
Propylene Oxide					
100	76	-24%	Hexene		
250	237	-5%	2	3.1	54%
500	492	-2%	8	8.8	10%
1000	1009	1%	17	15.2	-10%
			34	33.9	0%
Pentene			50	49.3	-1%
2	2	-23%	67	66.9	0%
8	8	-1%			
17	14	-18%	Pentanal		
34	32	-7%	50	43	-14%
50	51	1%	100	87	-13%
67	65	-3%	250	152	-39%
101	103	2%	500	523	5%
			1000	1015	1%
			5000	4160	-17%